

# CFD Analysis of Fuel Spray Characteristics inside a GDI Engine

K Santhosh Kumar

A Thesis Submitted to  
Indian Institute of Technology Hyderabad  
In Partial Fulfillment of the Requirements for  
The Degree of Master of Technology



Department of Mechanical Engineering

July 2013

## Acknowledgements

My sincere thanks to our guide Dr.Raja Banerjee who encouraged, motivated till end made me to complete this thesis work.

I thank my HOD Prof. Vinayak Eshwaran who constantly guide people in the right direction with his experience and made a bright future.

I also thank all the faculty Dr.Ashok panday sir, Dr. Venkata Subbaiah sir, Dr.Bhasker sir, Dr.Prashanth Kumar sir who transferred their knowledge during course work.

I also thank the Lab Incharge Madhu sir, Naga lakshmi Madam, Saritha Madam who constantly gave support sitting beside me in all the technical issues while running the simulation.

I thank all my friends in particular who look after me during placements and other information like power cuts, internet down even though I stayed outside the campus.

## Declaration

I declare that this written submission represents my ideas in my own words, and where ideas or words of others have been included, I have adequately cited and referenced the original sources. I also declare that I have adhered to all principles of academic honesty and integrity and have not misrepresented or fabricated or falsified any idea/data/fact/source in my submission. I understand that any violation of the above will be a cause for disciplinary action by the Institute and can also evoke penal action from the sources that have thus not been properly cited, or from whom proper permission has not been taken when needed.

K. Santhosh Kumar

(Signature)

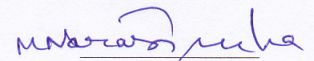
\_\_\_\_\_  
(Santhosh Kumar K)

me11m17

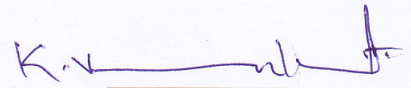
(Roll No.)

## Approval Sheet

This Thesis entitled CFD analysis of fuel spray characteristics inside a GDI engine by Santhosh Kumar K is approved for the degree of Master of Technology from IIT Hyderabad



(Dr.M Narasimha) Examiner  
Dept. of Chemical Eng  
IITH



(Dr.K Venkatasubbaiah) Examiner  
Dept. of Mechanical Eng  
IITH



(Dr.Raja Banerjee) Adviser  
Dept. of Mechanical Eng  
IITH



# Dedication

To Almighty Authority

## Abstract

The work produced discusses the analysis of gasoline atomization generated by different fuel injectors operating in a high pressure direct injection system. The simulation results of the influence of the fuel injection pressure and combustion chamber back pressure on the changes of the fuel spray geometrical parameters during the injection characterizing the injection quality such as injection penetration at different flow time have been presented in the paper. This study is based on dynamic mesh refinement and uses spray breakup models to simulate engine spray dynamics. It is known that the Lagrangian discrete particle technique for spray modeling is sensitive to grid resolution. An adequate spatial resolution in the spray region is necessary to account for the momentum and energy coupling between the gas and liquid phases. On the other hand, the accurate prediction of the spray structure and drop vaporization requires accurate physical models to simulate fuel injection and spray breakup. The present primary jet breakup model predicts the initial breakup of the liquid jet due to the surface instability to generate droplets. A secondary breakup model is then responsible for further breakup of these droplets. The secondary breakup model considers the growth of the unstable waves that are formed on the droplet surface due to the aerodynamic force. The simulation results are compared with experimental data obtained from literature (ILASS and ICLASS) in gasoline spray structure and liquid penetration length. Validations are also performed by comparing the liquid length of a vaporizing Gasoline spray and its variations with different parameters including the injection pressure, and ambient gas temperature and density. The model is also applied to simulate a direct-injection gasoline engine with a realistic geometry (with piston bowl , engine specifications such as bore to stroke ,compression ratio and volume of cylinder as standards)where piston is moving and spray injection at different CA (crank angle) location.The equivalence ratio contours are studied for better stratification at the time of spark for complete combustion to happen in turn increasing performance and decreasing engine emission. The present spray model with dynamic mesh refinement is shown to predict the spray structure and liquid penetration accurately with reasonable computational cost

# Contents

Acknowledgements . . . . .	ii
Abstract . . . . .	vi
<b>Nomenclature</b>	<b>vii</b>
<b>1 Introduction</b>	<b>4</b>
1.1 Emission regulation across the world . . . . .	4
1.2 The automotive industry response . . . . .	5
1.3 The Gasoline Direct Injection engines . . . . .	7
1.4 Combustion strategy . . . . .	7
1.5 Fuel mixing strategy for stratification . . . . .	9
1.6 The challenges of the GDI engine . . . . .	10
1.7 Objective . . . . .	12
1.8 Thesis Structure . . . . .	12
<b>2 Fundamentals of Mixture Formation in Engines</b>	<b>16</b>
2.1 Basics . . . . .	16
2.1.1 Break-Up Regimes of Liquid Jets . . . . .	16
2.1.2 Break-Up Regimes of Liquid Drops . . . . .	18
2.1.3 Atomization in Gasoline Sprays . . . . .	19
2.1.4 Structure of Engine Sprays . . . . .	20
2.2 Injection Systems and Nozzle Types . . . . .	24
2.2.1 Gasoline Engines . . . . .	24
<b>3 Modeling Spray and Mixture formation</b>	<b>27</b>
3.1 Primary Break-Up . . . . .	27
3.1.1 Blob-Method . . . . .	27

3.1.2	Sheet Atomization Model for Hollow-Cone Sprays . . . . .	30
3.2	Secondary Break-Up . . . . .	33
3.2.1	Taylor-Analogy Break-Up Model . . . . .	33
3.2.2	Kelvin-Helmholtz Break-Up Model . . . . .	33
3.2.3	Rayleigh-Taylor Break-Up Model . . . . .	35
<b>4</b>	<b>CFD Spray Model</b>	<b>37</b>
4.1	Numerical Simulation . . . . .	37
4.1.1	Transport Equations . . . . .	37
4.1.2	Euler- Lagrangian Model(Discrete Phase Model in Fluent terms) . . . . .	39
4.2	Phase coupling . . . . .	43
4.3	Results and Parametric Dependencies . . . . .	53
4.4	Dynamic or Deforming Mesh . . . . .	67
<b>5</b>	<b>Conclusion</b>	<b>85</b>





# Nomenclature

$\rho_l$	Density of Liquid
$\mu_l$	Dynamic Viscosity of Liquid
$\sigma$	Surface Tension on Droplet
$u_{rel}$	Relative Velocity between Liquid and Gas
MPa	Mega Pascals
D	Nozzle Diameter
L	Nozzle Length
PFI	Port Fuel Injection
GDI	Gasoline Direct Injection
$We_l$	Liquid Weber Number
$We_g$	Gaseous Weber Number
Re	Reynolds Number
Z	Ohnesorge Number
$P_{vap}$	Vapour Pressure of flow inside nozzle
$P_1 P_2$	Upstream and downstream pressures
DISI	Direct Injection Spark Ignition engine
$u_{inj}$	Injection Velocity
$m_{inj}$	Mass of Injection
$\omega$	Droplet wave Amplitude per unit time
$\Lambda$	Wavelength of Distorted Droplet
$\Omega$	Fastest Growing wave
r	Radius of Droplet
a	The radius of child Droplet
$\tau$	Breakup Time
$B_0 B_1$	Droplet breakup constants in relation finding breakup time
h	Enthalpy of Ideal gas
$T_{ref}$	Reference Temperature from where the <sup>2</sup> Integrals are done
$Sc_t$	Schmidt Number
$D_t$	Turbulent Diffusivity
$\theta$	Initial Spray Angle
$C_A$	Geometrical parameter in finding Initial Spray angle

$T_p$	Temperature of Particle
Nu	Nussult Number
$N_i$	Molar Flux of Vapor
$C_{i,s}$	Vapor Concentration on Droplet surface
$C_{i,1}$	Vapour Conentration in the bulk gas
$Sh_{AB}$	Sherwood Number
$M_{w,i}$	Molecular Weight of species i
$A_p$	Surface Area of Droplet
$K_1$	Thermal Conductivity of gas
$f_{v,0}$	Non-volatile fraction of Droplet
$T_{bp}$	Boiling point of fuel
ICLASS	International Conference on Liquid Atomization and Spray Systems
ILASS	Institute for Liquid Atomization and Spray Systems
$\nabla t$	Droplet flow time step
n	Number of Particle stream
SOI	Start of injection
S	Penetration Length
KHRT	Kelvin Helmholtz and Reyleigh Taylor Breakup model
TAB	Tayor Analogy Breakup Model
PDA	Phase Doppler Particle Anemometer
$\phi$	equivalence ratio
$\nabla\theta$	Injection Period
CA	Crank Angle

# Chapter 1

## Introduction

There is no doubt that the internal combustion engine has greatly benefitted our society. It has evolved from an unreliable, complicated machine to something easily use in nearly every mode of transportation. However, with this development also came unwanted side effects. The impact on the environment of the internal combustion engine first came to light in 1940s when the first serious air pollution was detected in California (Patterson and Henein 1972). As automobile traffic developed, so did this problem. In 1996, a report from the world health organization (WHO) estimated that particulate resulted in the premature death of 460,000 people each year (schwela 1996) in global scale.

### 1.1 Emission regulation across the world

In the United States, the national body for regulating emissions, the Environmental Protection Agency (EPA), was created in 1970. It introduced the Clean Air Act that set a national goal for a clean environment through exhaust emission reductions amongst other factors. California, which is the most populous state of the US, regularly experiences major pollution problems. As a result, it is the most aggressive in tackling pollution and the California Air Resources Board (CARB), a department of the Californian Environmental Protection Agency is responsible for the development of the Low Emission Vehicle (LEV) standard. This standard sets categories of vehicles according to the reduction in emission . These categories are ZEV (Zero Emission Vehicle), ULEV (Ultra-Low Emission vehicle), LEV and TLEV (Transitional Low-Emission Vehicle).



According to the LEV standard, car manufacturers must meet stringent emission targets and, from 2003, at least 10 percent of their vehicle sales must be ZEVs.

In Japan, another very densely populated country, the equivalent of the American Clean Air Act is the Japan Clean Air Program (JCAP). Up until 1990, Japan's emission regulation was one of the most stringent in the world, but has since fallen behind both US and Europe. Japan was one of the first countries to introduce unleaded gasoline.

In Europe, the first emission standards were drawn up by the UN Economic Commission for Europe (UNECE). However, since this body had no power of enforcement, it was up to the independent states to implement them or not. The first pan European regulations for emission performance were set up in 1988, with emission targets for gasoline and diesel cars according to their engine capacity. This resulted in the introduction of catalytic converters on large cars (> 2.0l) for the first time. In 1991, all engine capacities were regrouped in one category and emission targets were further tightened under the standard known as Euro I. Euro II, Euro III, Euro IV and Euro V were subsequently applied in 1996, 2000, 2005, 2009 respectively, and Euro VI is due to come into effect in 2013. Each of these standards is characterised by a drastic reduction in pollutant emission. Most countries elsewhere in the world follow one of the previous three regulation schemes. India, for example, implemented Euro I in 1996 for diesel engines and in 2000 for gasoline engines. It has implemented Euro II in 2000 for diesel engines, Euro IV in April 2010 and Euro VI is due to implement it in 2013 for gasoline ones for identified cities.

## 1.2 The automotive industry response

Consciousness in the environmental impact of the engine and the push of governments has led the automotive industry to spend considerable resources researching ways to improve engine emission and efficiency.

The manifold injection engine, introduced in the 1980s, was a step in this direction, and is now the standard for engines. The replacement of the carburettor with an injector placed in the engine manifold (port fuel injection, PFI) gives several advantages. The amount of fuel injected for each cycle can be better controlled, leading to fuel economy. Moreover, since the fuel flow is independent of the airflow, the engine can be operated at stoichiometric mixture across the whole load and speed map. At the same time, three way catalytic converters were introduced in order to reduce the

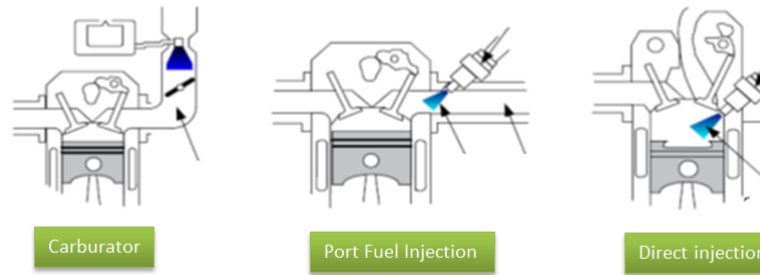


Figure 1.1: The mixture formation systems in GDI engines[1]

amount of hydrocarbon (HC), carbon monoxide (CO) and nitric oxide (NO<sub>x</sub>) present in the exhaust gases. These converters were designed in such a way that their efficiency was optimal with an engine running with a stoichiometric mixture.

However, three way catalytic converters are very sensitive to the mixture air-to-fuel ratio and their efficiency degrades rapidly for any deviation from stoichiometric (Ladommatos et al.1998).

The combination of port fuel injection and catalytic converters led to a significant decrease of emissions. Reduction in fuel consumption was also achieved by running the engine at less than stoichiometric air-to-fuel ratio, the lean-burn operation, under low-load or idle conditions. For example, a 10 percent reduction of the specific fuel consumption was achieved by running an engine at lean-burn conditions with sequential port injection combined with air-assisted injectors (Pontoppidan et al. 1998).

Many more improvements to the PFI engine have been designed since its conception. These include sequentially timed injection, computer algorithms for transient fuel metering, four valves per cylinder, multiple roller camshafts, variable cam phasing, turbocharging, supercharging, etc. Despite this, major improvements to emission and fuel emission performance is limited by two major problems intrinsic to this type of engine and shared by the carburettor engine: they require throttling for load control and they create a fuel film in the intake port. Throttling is a well-established and reliable method of load control. However since it reduces the amount of air entering the engine it is associated with substantial dynamic losses (Zhao et al. 1997).

As a result, the automotive industry turned its research effort towards the gasoline direct injection engine (GDI), which does not exhibit these two problems.

Table 1.1: Direct fuel injection for SI engines (various injector types and fuel pressures)[2]

No	Engine- type	Injector	Injection pressure
1	BMW HPI	Piezoelectric	20 MPa
2	Mercedes-Benz CGI	Piezoelectric	20 MPa
3	Volkswagen FSI	Electromagnetic	3-11MPa
4	Mitsubishi GDI	Electromagnetic	5 MPa
5	Renault IDE	Electromagnetic	10 MPa
6	Toyota D-4	Electromagnetic	4-13 MPa

### 1.3 The Gasoline Direct Injection engines

Though the port fuel injection system has some advantages, it cannot meet the increased demands of performance, emission legislation and fuel economy of the present day (Stone, 1999). The electronic controlled gasoline direct injection systems were started to be used instead of port fuel injection system since 1990s.

The Gasoline Direct Injection (GDI) engines give a number of features, which could not be realized with port injected engines: avoiding fuel wall film in the manifold, improved accuracy of air/fuel ratio during dynamics, reducing throttling losses during gas exchange ; higher thermal efficiency by stratified operation and increased compression ratio; decrease in the fuel consumption and  $CO_2$  emissions, lower heat losses, faster heating of the catalyst by injection during the gas expansion phase, increased performance and volumetric efficiency due to cooling of air charge, better coldstart performance and better drive comfort (Zhao et al., 1999; Karamangil, 2004; Smith et al., 2006).

### 1.4 Combustion strategy

Two different operating strategies are used with the GDI engine. The simplest strategy consists in employing homogenous stoichiometric operation over the entire load range. These engines then operate in early injection mode, where the fuel is injected during the intake stroke. These sort of engines does not fully realise the potential for fuel economy of the GDI engine as they still require throttling for fuel control, but combined with exhaust gas recirculation (EGR) and the charge cooling effect, they still manage good economy (Piccone et al. 1996). Their strength, however, is that they can use conventional after-treatment for emissions reduction. This combined with reduced cold-start emissions, fuel cut-off on deceleration and better transient response leads to greatly improved emissions performance compared to PFI. A more advanced combustion strategy that fully realises the potential of the direct injection is to operate the engine with a lean air-to-fuel ratio whenever

possible. As can be seen in Figure 1.2 there are typically three different operating modes:

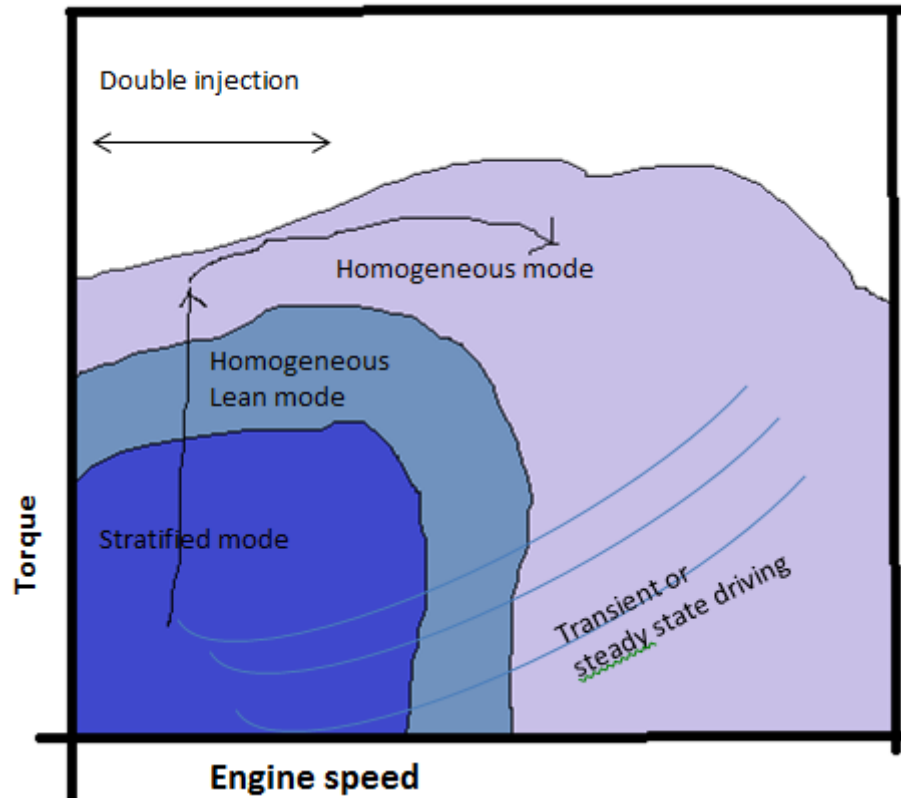


Figure 1.2: GDI engine operating modes depending on load and speed (Ksell et al., 1999).

1. Under low engine load, and low engine speed, the engine operates in stratified mode with very high air-to-fuel ratio ( $\gg 1$ ) and is unthrottled. In this mode, the overall mixture is lean (up to 40:1 air-to-fuel ratio) but the mixture is concentrated (stratified) around the spark plug and is thus inflammable. In order to achieve the stratification the fuel is typically injected late during the compression stroke. This strategy results in significant fuel economy as just enough fuel is injected to keep the engine running.

Furthermore since the engine is unthrottled, pumping losses are minimised, which also leads to smaller fuel requirements. A reduction in fuel consumption also means a reduction in pollutants (CO<sub>2</sub>) but also affects catalyst performance as the engine run scolder.

2. Under normal load, the engine operates in a homogeneous mode with a stoichiometric mixture and is throttled. The potential for fuel economy is reduced but is still present due to the EGR and charge cooling effect as mentioned above.
3. Under high load, the engine operates with a slightly rich mixture. Once again, the GDI benefits



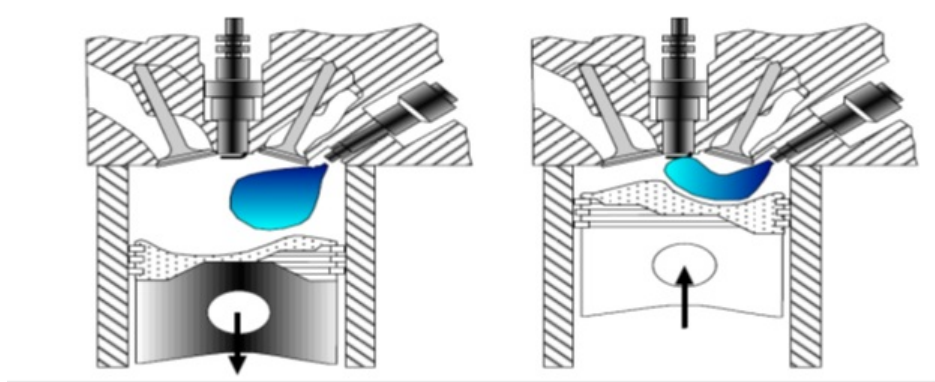


Figure 1.3: Homogeneous and stratified-charge mode[1]

since charge cooling is still present.

The disadvantage of using stratified operation is that special exhaust gas after treatment is required, as current systems do not cope well with lean mixtures. The combination of stratification and homogenous mode means (Fig1.3), however, that their use can be balanced to give very good fuel economy with acceptable emission performance when possible and good emission performance with acceptable fuel economy otherwise.

## 1.5 Fuel mixing strategy for stratification

Three major fuel-mixing strategies have been developed in order to realise the fuel stratification. These are known as air guided, wall guided and spray guided according to the dominant phenomenon that governs the stratification and are shown in Fig1.4 (Preussner et al. 1998). It must be noted that despite this denomination, the air and fuel mixing is the result of a combination of these phenomena. Their relative importance, however, varies according to the strategy.

Spray guided systems are characterised by a special arrangement where the spark plug and injector are located close together. The air-to-fuel ratio is controlled by the penetration of injected spray and is thus mainly determined by the spray physics. This strategy only allows for limited stratification. Moreover, due to the proximity of the spark plug and injector, spark plug wetting becomes a problem, leading to shortened lifetime of the spark plug or to higher costs for more resistant materials. The spray-guided system is the least common. It can however achieve very high air-to-fuel ratios under idling load, up to 115:1 (Stutzenberg et al. 1996).

In the wall-guided system, the fuel is directed toward the spark plug by the shape of the piston. In this case, the inlet ports are usually designed so that the airflow enters the chamber in a top-

down direction (top-entry design) and the piston crown is shaped like a bowl (bowl-in piston). The top-entry design results in an in-cylinder flow that rotates in a plane parallel to piston axis (tumble plane). In addition to redirecting the fuel toward the spark plug, the wall-guided strategy has the advantage of accelerating the rotation of the air flow due to compression. This creates high levels of near-wall flow velocities even late in the compression stroke, which promotes the evaporation of the fuel film formed by impingement of the spray on the walls. The tumble motion also helps transporting the fuel toward the spark plug. There are two variations of the top entry design, resulting in two different directions of the air flow rotation, depending on the location of the injector relative to the intake valve. If the injector is located below the intake valve, the flow is directed downward against the cylinder wall. This is called reverse tumble (Lake et al. 1996). In contrast, tumble is generated for injectors above the intake valve where the flow is directed toward the centre of the cylinder (Krmer et al. 1997b). The wall-guided system was first designed by Mitsubishi (Kume et al. 1996) and Ricardo (Jackson et al. 1997) and has subsequently been intensively applied.

In the air-guided system, the fuel is directed toward the spark plug by the airflow inside the cylinder. The inlet ports are designed so that they create an air flow that rotates around the spark plug in a plane perpendicular to the piston axis (swirl plane). Different methods of achieving this phenomenon include different valve lift for the intake valves, helical inlet ports, valves shrouds, all designed to direct the airflow in a rotation around the piston axis.

Furthermore, the piston often includes a cylindrical bowl or other shape cavity designed to impart a radial motion to the air flow as the piston nears top dead centre, so that once again the fuel is concentrated around the spark plug. The advantage of the air-guided system is that the swirl motion is preserved for longer during compression and thus helps to maintain the mixture stratification until ignition. However, it also has the potential of sending the largest droplets from the fuel spray toward the cylinder wall due to the centrifugal force resulting in fuel wall wetting. This is a problem as fuel deposited on the wall will cool down and get trapped in piston crevices resulting in poor combustion and hence an increase in pollution.

## 1.6 The challenges of the GDI engine

As has been seen, the lean operation of the engine by stratifying the fuel mixture has great potential for fuel economy. However, to achieve good performance, it must be ensured that a stoichiometric mixture surrounds the spark plug at ignition time, otherwise knock and misfire can occur. Therefore, the air and fuel mixing is of utmost importance to the good operation of the GDI engine. Even, when

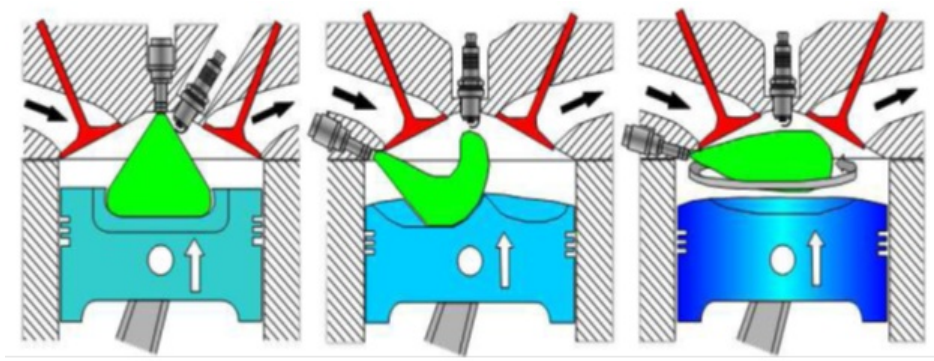


Figure 1.4: The wall-guided, air-guided and spray-guided combustion systems at stratified charge (Stefan, 2004)

operating under overall stoichiometric mode, the mixing is critical as after treatment performances are dependent on the air-to-fuel ratio.

The mixing process is dependent upon several components all linked together: fuel injection, air motion, engine design and evaporation process. The fuel injection process, characterized by injection duration, injection timing (early for homogeneous, late for stratified), injection pressure and the injector physical characteristics, is one of these. The aim is to atomise the fuel as best as possible to minimise wall wetting and obtain a fully evaporated fuel mixture at ignition time. Injector tip shape, injector needle lift, spray shape (hollow or full), spray cone angle, fuel droplet diameter, spray penetration, all play an important role in the fuel injection process and all must be chosen carefully. The amount of turbulence and the air flow velocity is critical to the functioning of the GDI engine. When operating under homogeneous mode, high turbulence combined with low mean velocity near the spark plug are required, whereas under stratified mode, the opposite is required. As has been explained before, the direction of the air flow together with its behaviour under compression is crucial in achieving good mixture stratification and good fuel evaporation. The shape of the combustion chamber, the location of the spark plug and injector, the orientation and shape of the intake ports also play an important role. The fuel evaporation process is the last crucial parameter in determining the mixing process and is dependent on the other three.

Understanding and characterising the air and fuel mixing process is critical to developing direct injection engines that operate correctly and is necessary for further improvement. In particular, studying the fuel distribution and its evolution prior to ignition is important in assessing the fuel mixing. Therefore, the main objective of the work in this thesis is to develop a technique for quantitative assessment of the penetration depth in the cylinder of a GDI engine, with good spatial and temporal resolution.

## 1.7 Objective

The principal objective of the work described in this thesis was to investigate and develop a method for the measurement of quantitative , three-dimensional in-cylinder spray characteristics like penetration depth with different injectors in a model direct injection engine using the DPM (Discrete phase model) technique. The main steps of the project were to:

1. Gain a thorough understanding of the DPM technique , GDI engine advantages and various injectors used through a literature review.
2. Select and procure the software needed for the application of the DPM technique to an internal combustion engines.
3. Gain a practical experience of the technique and understanding of the equipment by going through experiments conducted on spray analysis.
4. Develop a calibration technique for quantitative measurement of spray penetration at various ambient conditions, and also by varying flow and geometrical parameters
5. Apply the calibration method to analyze engine behavior and compare with test or experimental data.

## 1.8 Thesis Structure

The structure of the present thesis closely follows the objective described in the previous section. The remainder of the Chapter 1 , the introduction , concentrates on the outlining the necessity of a technique for quantitative in-cylinder spray penetration measurement . Chapter 2 present a literature survey on the techniques for in-cylinder focusing mostly on the type of injectors, spray ambient conditions and geometrical parameters. The concept of injecting liquid through a small hole may seem a trivial process, but the physics of spray formation proves to be extremely complex. Although the analysis of liquid spray formation is a science discipline on its own, understanding some of its physical aspects is already valuable for numerical modeling. In the further sections the fundamentals of liquid sprays in general, like spray regimes, droplet formation and breakup regimes, are presented. The Table 1.2 gives the thermo-physical properties of materials and the Table 1.3 will give the idea of all parameters required for the injection system in working with GDI injection system. Table 1.4 with references gives Experimental procedures had done on GDI engine . Table 1.5 give us the information on Fuel composition for the Gasoline and Diesel fuel. Chapter 2 describes the

theory behind the development of spray models for IC (Gasoline) engines. Chapter 3 describes the breakup models such as primary and secondary breakup models. Chapter 4 describes the governing equation for continuous phase and discrete phase calculation, Coupling between the two phases by exchange of mass, momentum and energy. Model settings for the simulation software (Fluent). The tables below give some idea of Literature survey that has been done on spray models to complete this very little amount of work.

Table 1.2: Fuel properties [14]

	n-Hexane	n-Heptane	n-octane	n-Decane	3-comp	Gasoline
0.1 MPa, 25 <sup>0</sup> C						
Density (kg/m <sup>3</sup> )	636	664	694	717	705	720 to 740
Surf tens (nN/m)	66	99	100	174	66 to 174	35 to 200
Kine visc – 10 <sup>6</sup> (m <sup>2</sup> /s)	17.89	19.65	18.33	23.37		22.00
Vap press (kPa)	0.446	0.583	2.874	1.210	0.568	0.530
Ref index	19.90	6.06	6.58	1.71		50 to 60
Heat of evap (kJ/kg)	1.375	1.388	1.391	1.409	1.385	1.427
1.5 MPa, 70 <sup>0</sup> C						
Density (kg/m <sup>3</sup> )	618	630	659	690	638	695
Vapor temp (0C)	190	226	233	321		
Surf tens (nN/m)	13.27	15.24	14.33	19.23	15.35	17.6
Kine visc 10 <sup>6</sup> (m <sup>2</sup> /s)	0.337	0.405	2.427	0.730		
Vap press (kPa)	104	40.4	40.8	2.38		210
Ref index	1.352	1.365	1.370	1.395	1.370	1.410
Heat of evap (kJ/kg)	328.3	330.2	280.3	329.9		

Table 1.3: From the following papers the data required for present study was shown in a tabular form

Vol Year Aut	Fuel	Injector Type	Amb Cond	Mesh cell size	Inj oper cond	Software Exp method
[3]	Diesel	Plain orifice Atomizer	950K, 2.45MPa	1mm3	$T_f = 323K$ , mf=0.0088 Kg/s, D=177m, L=1mm	Fluent / TU/e, IFP, Sandia
[4]	Iso-octane	Press swirl Atomizer	Amb cond	1mm3	Pinj=8,10MPa, mf=vary, D=0.5mm, Cone angle=67 <sup>0</sup> , t=3ms	StarCD/ PIV, PDA
[5]	Dodecane	Solid cone	300K, 1.1, 3,5MPa	2.5mm3	$M_f = 6.05$ , 5.36, 5.13 g/s, D=0.3mm, $V_{inj} = 102, 90$ , 86 m/s, $\frac{\theta}{2} = 7.5$ , 12.4,16 <sup>0</sup>	Fluent/ LSI, PDA
[6]	Iso-octane	Cone	Amb conditions	1mm3	Pinj=8, 10MPa, mf=vary, R=0.00045mm, Cone angle = 28 <sup>0</sup> , Start = 250 <sup>0</sup> CA End = 355 <sup>0</sup> CA	Fluent
[7]	C8H17	Hollow cone	————	————	Ref	KIVA-3V

Table 1.4: Experimental papers

Experiment Method	Injector Used	Fuel	Conditions and parameters of equipment	Ref Number
RAINBOW SCHLIEREN DEFLECTOMETRY, ULTRA HIGH SPEED IMAGING		Hydrogen	$Vol_{cham} = 300cm^3$ , $Inj_{press} = 275.8$ kPa (40 psi) 413.7 kPa (60 psi) and 551.6 kPa (80 psi)	[14]
PHASE DOPPLER ANEMOMETRY			Amb temp ( $20^0C$ ) and ( $-60^0c$ )	[13]
3D PARTICLE TRACKING VELOCIMETRY			Ref	[12]
laser phase -Doppler anemometry(PDA)			Ref	[11]
laser elastic light scattering	Single hole injector	Nitrogen	$T_a = 520$ K, $P_f = 100$ MPa, $P_a = 4$ MPa	[10]
DENSO fuel injection equipment	Multihole injector	Diesel	Ref	[9]
Kodak Ektapro high-speed image Analyser (Model 4540)	VCO and Mini-sac single and multihole	Diesel	Ref	[8]

Table 1.5: Fuel Composition

Title	Fuel Composition	Reference
Motor Gasolines Technical Review	Gasoline	[15]
Standards for the Composition of Automobile Gasoline and Diesel Fuels	Gasoline and Diesel	[16]

## Chapter 2

# Fundamentals of Mixture Formation in Engines

### 2.1 Basics

#### 2.1.1 Break-Up Regimes of Liquid Jets

Dependent on the relative velocity and the properties of the liquid and surrounding gas, the break-up of a liquid jet is governed by different break-up mechanisms. These different mechanisms are usually characterized by the distance between the nozzle and the point of first droplet formation, the so-called break-up length, and the size of the droplets that are produced. According to Reitz and Bracco [17], four regimes, the Rayleigh regime, the first and second wind-induced regime, and the atomization regime, can be distinguished which can be seen in Fig 2.1

In order to give a quantitative description of the jet break-up process, Ohnesorge [18] performed



Figure 2.1: Schematic description of jet break-up regimes [18]



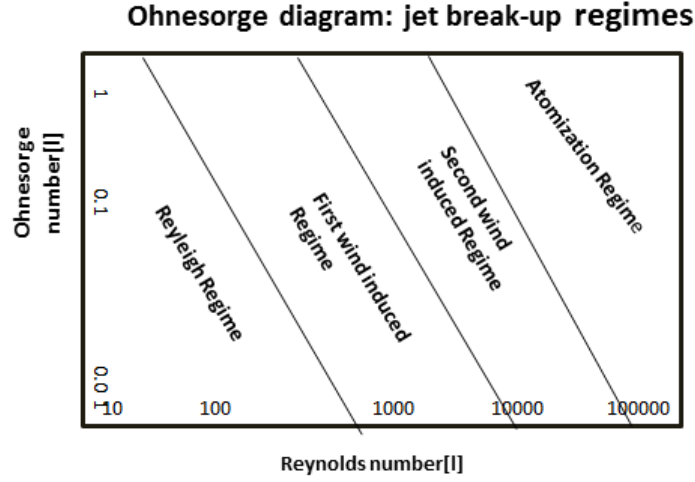


Figure 2.2: Ohnesorge diagram: jet break-up regimes and the Reynolds number [18]

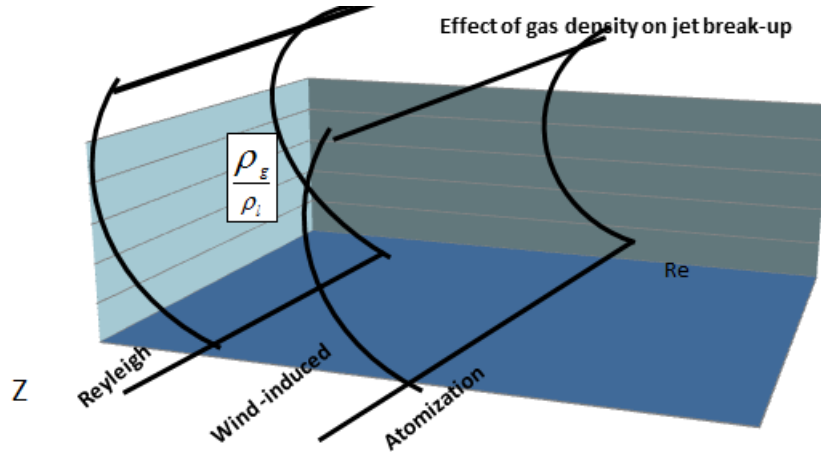


Figure 2.3: Schematic diagram including the effect of gas density on jet break-up [18]

measurements of the intact jet length and showed that the disintegration process can be described by the liquid Weber number

$$We_l = \frac{u^2 D \rho_l}{\sigma} \quad (2.1)$$

$$Re = \frac{u D \rho_l}{\mu_l} \quad (2.2)$$

Eliminating the jet velocity  $u$ , Ohnesorge derived the dimensionless Ohnesorge number,

$$Z = \frac{\sqrt{We_l}}{Re} = \frac{\mu_l}{\sqrt{\sigma \rho_l D}} \quad (2.3)$$

which includes all relevant fluid properties  $\sigma$ : surface tension at the liquid-gas interface  $\rho_l$ : density

Table 2.1: Transition Weber numbers of the different drop break-up regimes

Wierzba [19]	Weber number	Arcoumanis et al. [20]	Weber number
Vibrational	= 12	Vibrational	= 12
Bag	< 20	Bag	< 20
Bag-jet (Bag-streamer)	< 50	Stripping Sheet stripping	< 100 < 350
Stripping	< 100	Wave crest Stripping	< 1000
Catastrophic	> 100	Catastrophic	> 1000

of liquid  $\mu_l$ :dynamic viscosity of liquid as well as the nozzle hole diameter D. Fig.2.2 shows the Ohnesorge diagram, where Z is given as a function of Re. For stationary conditions, the boundaries between the four different jet break-up regimes can be drawn in. Thus, Reitz [16] suggested to include the gas-to-liquid density ratio and to extend the two-dimensional Ohnesorge diagram into a three-dimensional one as shown in Fig.2.3.

### 2.1.2 Break-Up Regimes of Liquid Drops

The break-up of drops in a spray is caused by aerodynamic forces (friction and pressure) induced by the relative velocity  $u_{rel}$  between droplet and surrounding gas. The aerodynamic forces result in an instable growing of waves on the gas/liquid interface or of the whole droplet itself, which finally leads to disintegration and to the formation of smaller droplets. These droplets are again subject to further aerodynamically induced break-up. The surface tension force on the other hand tries to keep the droplet spherical and counteracts the deformation force. The surface tension force depends on the curvature of the surface: the smaller the droplet, the bigger the surface tension force and the bigger the critical relative velocity, which leads to an instable droplet deformation and to disintegration. This behavior is expressed by the gas phase Weber number,

$$We_g = \frac{u^2 D \rho_g}{\sigma} \tag{2.4}$$

where d is the droplet diameter before break-up,  $\sigma$  is the surface tension between liquid and gas,  $u_{rel}$  is the relative velocity between droplet and gas, and  $\rho_g$  is the gas density. The Weber number represents the ratio of aerodynamic (dynamic pressure) and surface tension forces. From the Fig.2.4 we get some idea of different drop breakups and Table 2.1 will give idea on breakup regimes corresponding to Weber Number.




















Vibrational break-up	→				
Bag break-up	→				
(Bag-streamer) break-up	→				
Stripping break-up	→				
Catastrophic break-up	→				

Figure 2.4: Drop break-up regimes according to Wierzba [19]

### 2.1.3 Atomization in Gasoline Sprays

Modern injectors for Gasoline engines have nozzle diameters of  $200 \mu\text{m}$  or less, and the length of the nozzle hole is approximately 1 mm. Injection pressures up to 200 MPa are used and therefore the jet velocity  $u$  reaches values of 500 m/s and more. These conditions result in an atomization regime for the primary breakup mechanism. Some possible sources for atomization are shortly treated in the following.

**Aerodynamic shear** Aerodynamic shear forces amplify the surface waves created by the turbulence in the nozzle hole. The waves separate from the jet and form droplets. There are two reasons why this aerodynamic source is less important. First, this process is time dependent, but it is known from experiments that jets break immediately at the exit of the nozzle. Second, aerodynamic breakup is a surface effect, so it cannot explain disintegration of the inner structure.

**Relaxation of velocity profile** At the wall inside the nozzle a no-slip boundary conditions exists, forcing the flow towards a Poiseuille velocity profile. When the liquid exits the nozzle, the velocity profile will transform into a uniform one. In order to realize that the outer region of the liquid accelerates, which may cause instabilities and ultimately result in breakup into droplets. However, in modern diesel engines the length to diameter ratio of the nozzle hole is typically small ( $[\frac{L}{D}]_{nozzle} = 5$ ), so probably the flow in the nozzle has no time to develop.

**Turbulence** The presence of radial turbulent velocity fluctuations in the jet results, if strong

enough to overcome the surface tension, in formation of droplets. Turbulence-induced primary breakup is considered one of the most important mechanisms in high pressure applications.

**Cavitation** Cavitation is the transition from liquid to gas due to the decrease of static pressure below the vapor pressure. The curved streamlines at the upstream edge of the nozzle result in a radial pressure gradient. So, at places where the pressure is lower than the vapor pressure, cavitation bubbles are formed. These bubbles in the liquid flow contribute to primary breakup since they implode when they enter the high pressure environment. Parameters that influence cavitation are the upstream nozzle edge and the angle between the injector needle axis and the nozzle hole axis. A sharper edge results in stronger cavitation, which in turn results in smaller ligaments and a larger cone angle. If the angle between the needle and the hole is too large, the flow in the nozzle and also the spray is asymmetric due to the asymmetry of the streamlines. Although cavitation is strongly dependent on the injector/nozzle geometry, the cavitation number  $K$  is an important dimensionless parameter to predict the inception of cavitation. The cavitation number is defined as follows:

$$K = \frac{P_1 - P_{vap}}{P_1 - P_2} \approx \frac{P_1}{P_1 - P_2} \quad (2.5)$$

The indices 1 and 2 refer to the upstream and downstream pressures respectively and  $p_{vap}$  is the vapor pressure of the liquid. Since in automotive applications  $P_{vap} \ll P_1$  the vapor pressure may be eliminated from equation (2.5).  $K$  is defined such that it decreases with increasing cavitation intensity. To include the influence of the geometry, an empirical criterium is used to decide when cavitation occurs. This and more about computational considerations are treated in the following chapters.

## 2.1.4 Structure of Engine Sprays

### Full-Cone Sprays

A schematic description of a full-cone high-pressure spray is given in Fig.2.5. The graphic shows the lower part of an injection nozzle with needle, sac hole, and injection hole. Modern injectors for passenger cars have hole diameters of about  $180\mu\text{m}$  and less, while the length of the injection holes is about 1 mm.

The Fig 2.6 and Fig 2.7 Gives us the idea on spray penetration axially and radially.

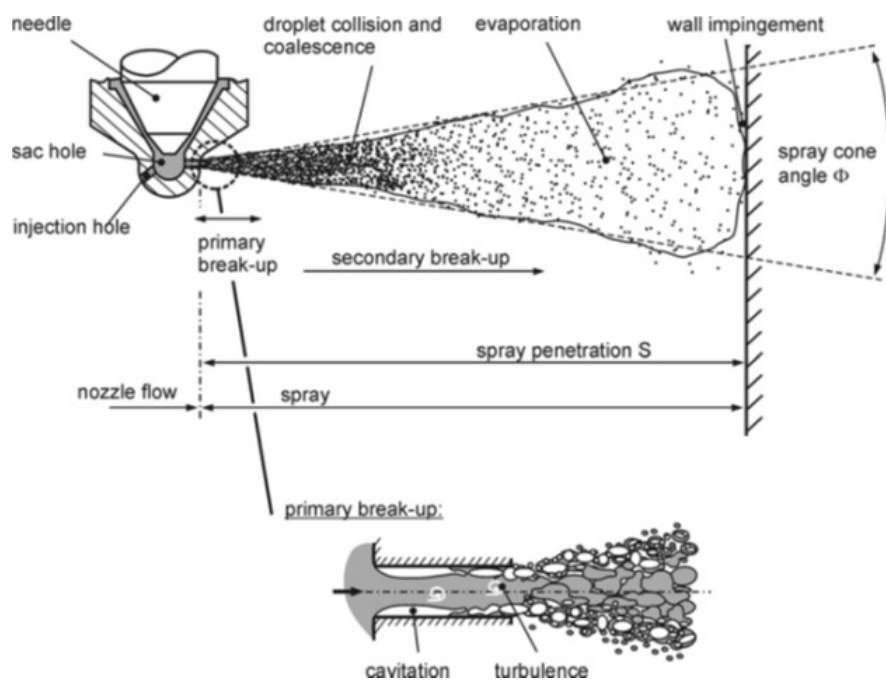


Figure 2.5: Break-up of a Solid-cone Gasoline spray[3]

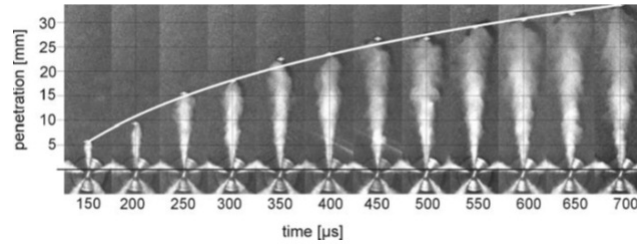


Figure 2.6: Spray development during injection [21],  $P_{rail} = 70MPa$ ,  $P_{back} = 5MPa$ ,  $T_{air} = 890K$

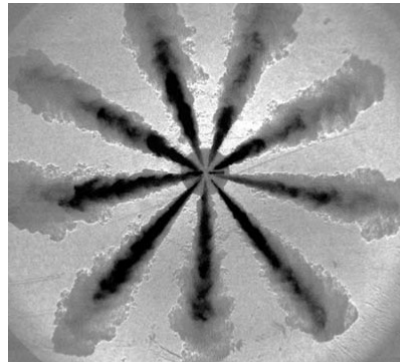


Figure 2.7: Distribution of liquid (black) and vapor (gray) in an evaporating high-pressure diesel spray from a multi-hole nozzle under engine like conditions. Measurement technique: superposition of Schlieren technique (vapor and liquid) and Mie scattering (liquid) y [21]

### Hollow-Cone Sprays

In order to achieve maximum dispersion of the liquid at moderate injection pressures and low ambient pressures, hollow-cone sprays are usually used. Hollowcone sprays are typically characterized by small droplet diameters, effective fuel air mixing, reduced penetration, and consequently high atomization efficiencies. These sprays are used in conventional gasoline engines, where the fuel is injected into the manifold, and in direct injection spark ignited (DISI) engines as well.

Fig. 2.8 shows the typical structure of such a spray. The liquid emerging from the nozzle forms a free cone-shaped liquid sheet inside the combustion chamber, which thins out because of the conservation of mass as it departs from the nozzle and subsequently disintegrates into droplets. Two nozzle concepts exist: the inwardly opening pressure-swirl atomizer and the outwardly opening nozzle. In the case of a swirl-atomizer, a cylindrical and strongly rotating liquid film leaves the nozzle. The radial velocity component, which is caused by the rotational motion, results in the formation of the free cone-shaped liquid sheet. In the case of an outwardly opening nozzle, the geometry of the needle causes the liquid to form the cone-shaped liquid sheet.

### Pre-spray

Due to the small flow velocity inside the nozzle at the beginning of injection, the first amount of

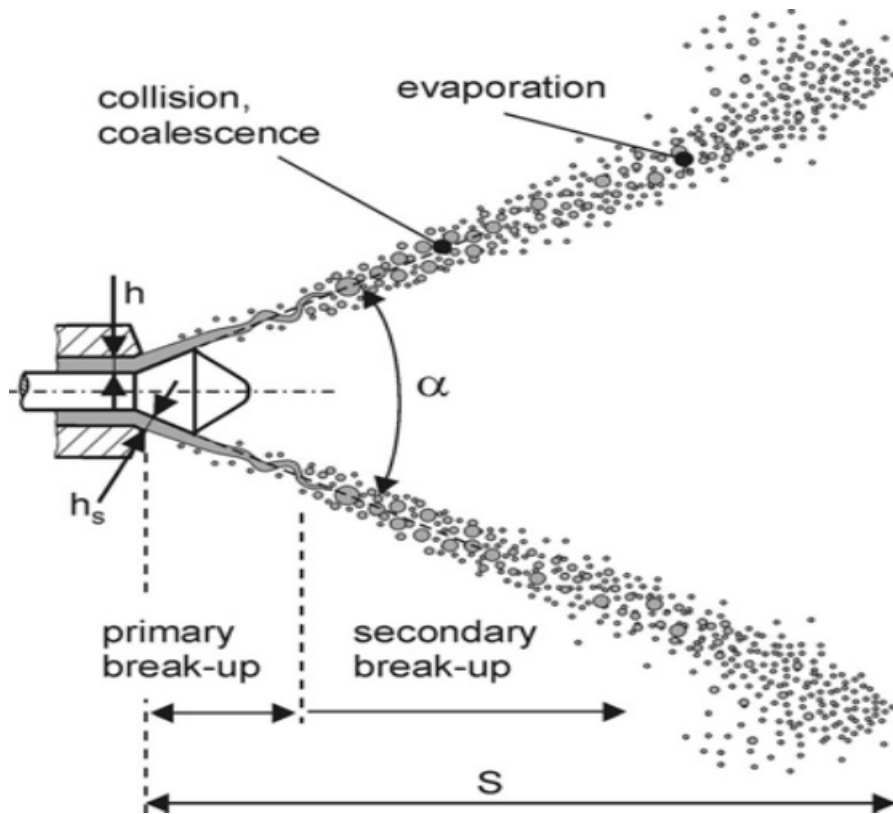


Figure 2.8: Hollow-cone spray. Example: outwardly opening nozzle

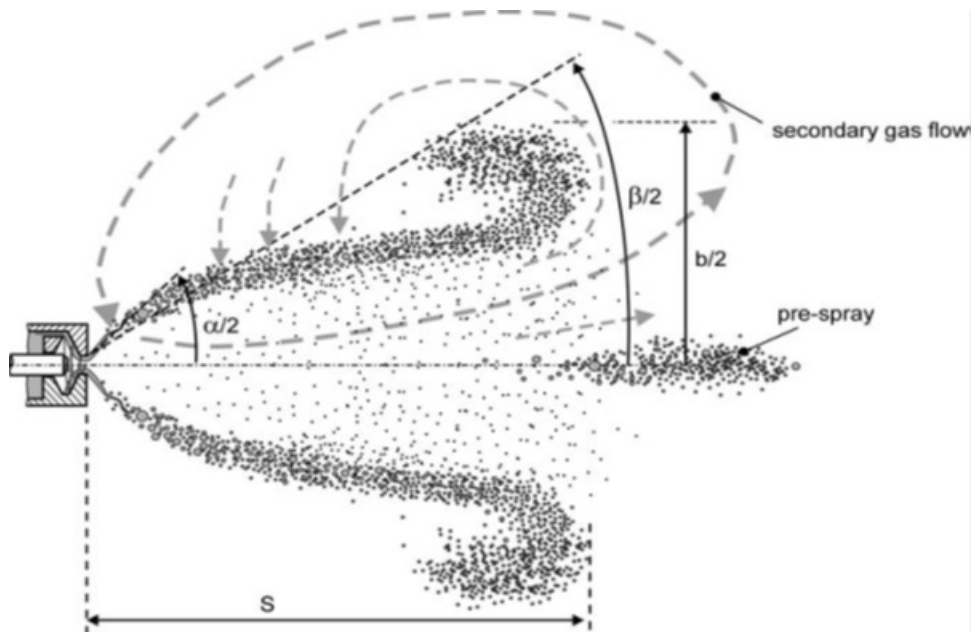


Figure 2.9: Typical spray from a pressure-swirl atomizer (Example: Inwardly opening hollow cone spray schematic illustration)

fuel entering the swirl chamber inside the nozzle does not receive sufficient rotational motion, leaves the nozzle with nearly zero swirl, and forms a kind of solid-cone spray with narrow spray cone angle and large drops, the so-called pre-spray. As the fuel velocity increases, the liquid inside the swirl chamber forms a hollow-cylinder structure. This structure is then transformed into a hollow-cone spray as it leaves the nozzle. The hollow-cone spray starts to penetrate into the gas atmosphere with an initial cone angle  $\theta$ , illustrated in Fig. 2.9

## 2.2 Injection Systems and Nozzle Types

### 2.2.1 Gasoline Engines

#### Direct Injection

The first kind of nozzle is the multi-hole nozzle. The functional principle as well as the shape and structure of the individual sprays produced by each hole are well-known from the high-pressure diesel injection. This nozzle produces a number of compact sprays with relatively large penetration (low gas density) and large droplet sizes (low injection pressure compared to diesel applications). Hence, the overall spray is strongly inhomogeneous, consisting of fuel-rich zones that are separated by very lean regions, Fig. 2.10

The other two nozzle categories, the outwardly opening nozzle and the inwardly opening pressure-swirl injector, produce a hollow-cone spray. The key advantage of hollow-cone sprays over solid-cone sprays is the high area-to-volume ratio, which leads to the required level of atomization without large penetration.

In a high-pressure swirl atomizer, the fuel passes through tangentially arranged swirl ports and gets a rotational motion inside the swirl chamber, Fig. 2.12. The centrifugal motion of the liquid forms a hollow air core. Because the area of the swirl chamber reduces to a nozzle, the rotational motion is further increased. The liquid passes through the nozzle and forms a free cone-shaped liquid sheet inside the combustion chamber, which thins because of the conservation of mass as it departs from the nozzle and subsequently disintegrates into droplets.



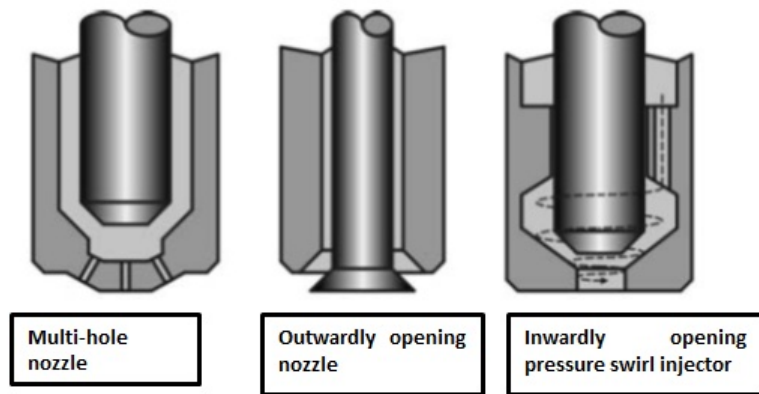


Figure 2.10: Direct injection of gasoline: injector geometries

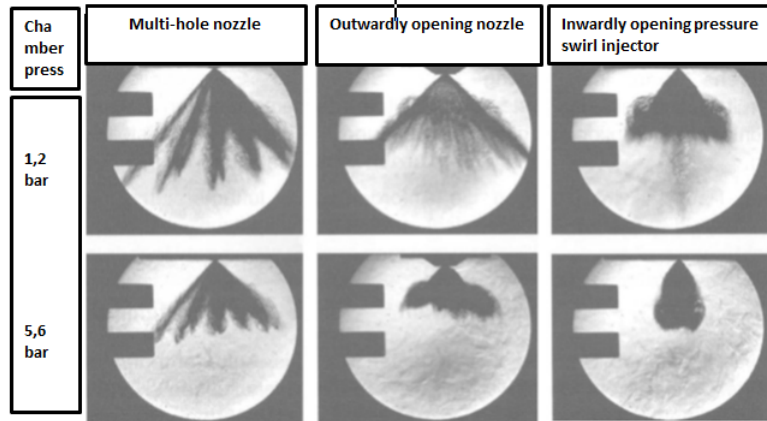


Figure 2.11: Effect of injection pressure on the spray structure [19],  $P_{rail} = 10MPa$

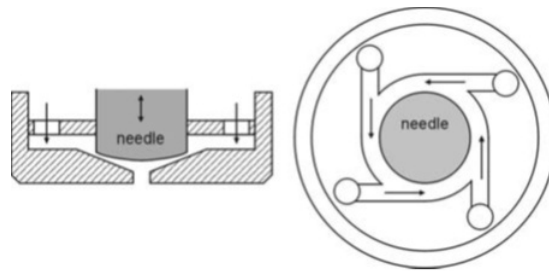


Figure 2.12: Example of a high-pressure swirl atomizer with tangentially arranged swirl ports [19]

## Chapter 3

# Modeling Spray and Mixture formation

### 3.1 Primary Break-Up

The primary break-up process provides the starting conditions for the calculation of the subsequent mixture formation inside the cylinder, and for this reason a detailed modeling of the transition from the nozzle flow into the dense spray is essential. Because the Lagrangian description of the liquid phase requires the existence of drops, the simulation of spray formation always begins with drops starting to penetrate into the combustion chamber. The task of a primary break-up model is to determine the starting conditions of these drops, such as initial radius and velocity components (spray angle), which are mainly influenced by the flow conditions inside the nozzle holes.

#### 3.1.1 Blob-Method

The simplest and most popular way of defining the starting conditions of the first droplets at the nozzle hole exit of full-cone Gasoline sprays is the so-called blob method. This approach was developed by Reitz and Diwakar [22]. The blob method is based on the assumption that atomization and drop break-up within the dense spray near the nozzle are indistinguishable processes, and that a detailed simulation can be replaced by the injection of big spherical droplets with uniform size, which are then subject to secondary aerodynamic-induced break-up, see Fig.3.1.

The diameter of these blobs equals the nozzle hole diameter  $D$  (mono-disperse injection) and the number of drops injected per unit time is determined from the mass flow rate. Although the blobs

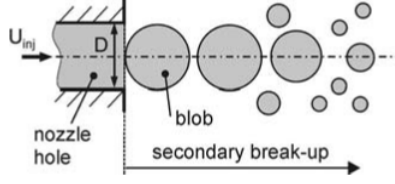


Figure 3.1: Blob Method

break up due to their interaction with the gas, there is a region of large discrete liquid particles near the nozzle, which is conceptually equivalent to a dense core. Assuming slug flow inside the nozzle hole, the conservation of mass gives the injection velocity  $U_{inj}(t)$  of the blobs

$$U_{inj}(t) = \frac{m_{inj}(t)}{A_{hole}\rho_l} \quad (3.1)$$

where  $A_{hole} = \pi D^2/4$  is the cross-sectional area of the nozzle hole,  $\rho_l$  is the liquid density, and  $m_{inj}(t)$  is the fuel mass flow rate (measurement). If there are no measurements about the injected mass flow, the Bernoulli equation for frictionless flow can be used in order to calculate an upper limit of the initial velocity,

$$U_{inj,max} = \sqrt{\frac{2\Delta P_{inj}}{\rho_l}} \quad (3.2)$$

where  $\Delta P_{inj}$  is the difference between the sac hole and combustion chamber pressures. Because the flow is not frictionless,  $U_{inj,max}$  is reduced by energy losses.

At the beginning and end of injection, the flow is usually turbulent, the blob size equals the nozzle hole diameter  $D$ , and the injection velocity is calculated using Eq. 3.1. During the main injection phase, the flow is usually cavitating, see Fig. 3.2. In this case, the effective cross-sectional area of the nozzle hole exit  $A_{eff}$  is smaller than the geometrical area. A hole resulting in a decrease of the blob diameter,

$$D_{eff} = \sqrt{\frac{4A_{inj}}{\pi}} \quad (3.3)$$

while the injection velocity is increased. A momentum balance from the vena contracta (point 1) to the hole exit (point 2), together with the conservation of mass

$$m_{inj} = \rho_l u_{vena} A_{hole} C_c = \rho_l u_{eff} A_{eff} \quad (3.4)$$

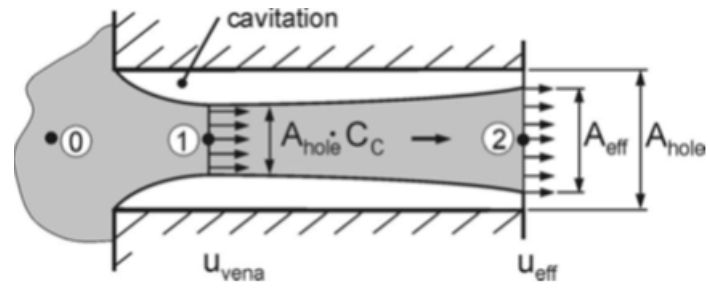


Figure 3.2: One-dimensional cavitating nozzle hole flow

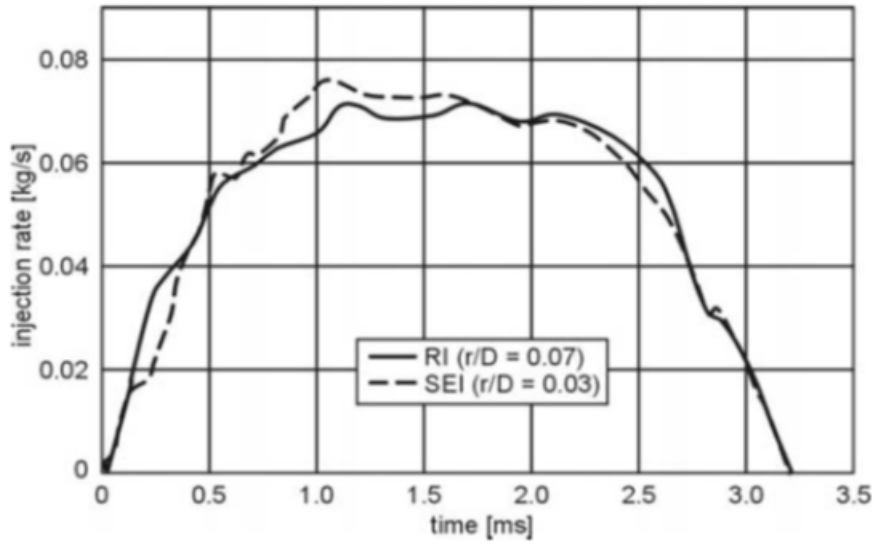


Figure 3.3: Injection profiles for sharp-edged (SEI) and round-edged inlet (RI),

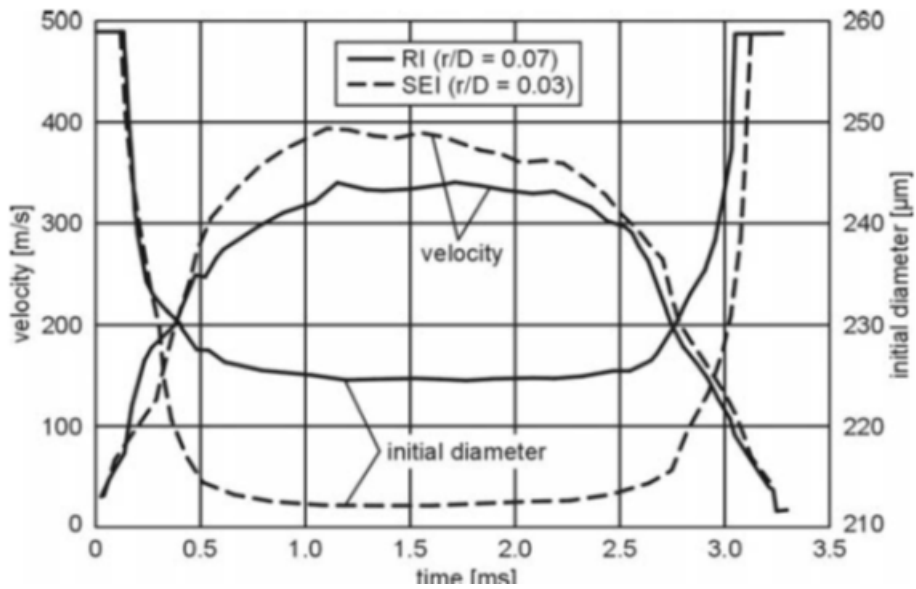


Figure 3.4: Dynamic calculation of blob diameter and injection velocity, data from

gives the injection velocity

$$U_{eff} = \frac{A_{hole}}{m_{inj}}(P_{inj} - P_2) + u_{vena} \quad (3.5)$$

where

$$U_{vena} = \frac{m_{inj}}{\rho_l A_{hole} C_c} \quad (3.6)$$

The effective flow area in Eq. 3.3 is

$$A_{eff} = \frac{m_{inj}}{U_{eff} \rho_l} \quad (3.7)$$

Fig 3.2 and 3.3 show an example of the dynamic calculation of initial blob diameter and injection velocity based on the measured mass flow through a sixhole injector ( $D = 259\mu m$ ) with either a sharp-edged inlet (SEI) or a round-edged inlet (RI). Because of the small mass flows and injection velocities at the beginning and at the end of the injection process, the injection starts and ends with blobs having a diameter equal to  $D$ . As soon as cavitation is predicted, the initial diameter decreases rapidly. The highest velocities and the smallest blob diameters are predicted during the main injection process. Compared to the original blob-method, the dynamic calculation of blob size and injection velocity during the whole injection event introduces the effect of cavitation by decreasing the initial blob size and estimating a more realistic initial velocity. However, only the passive effect of cavitation, the reduction of flow area, is considered. The increase of turbulence and break-up energy due to cavitation bubble implosions is not included.

Altogether, the blob method is a simple and well-known method of treating the primary break-up in Eulerian-Lagrangian CFD codes. As far as there is no detailed information about the composition of the primary spray, and measurements about the spray cone angle are available, it is the best way to define the initial starting conditions for the liquid entering the combustion chamber. Nevertheless, this method does not represent a detailed physical and satisfying modeling of the relevant processes during primary break-up. The most important disadvantage is that the influence of the 3D nozzle hole flow on 3D spray angle and drop size distribution cannot be mapped and that the promotion of primary break-up by turbulence and by implosions of cavitation bubbles outside the nozzle is not regarded at all.

### 3.1.2 Sheet Atomization Model for Hollow-Cone Sprays

Compared to the boundary conditions in the case of diesel engines, the backpressures and temperatures are small and the use of full-cone sprays would result in poor mixture formation and increased

wall impingement. Hollow-cone sprays are typically characterized by small droplet diameters, effective fuel-air mixing, reduced penetration, and thus high atomization efficiencies. Fig. 3.5 shows two nozzle concepts, an inwardly opening pressure-swirl atomizer and an outwardly opening nozzle. In case of a swirl-atomizer, the fuel passes through tangentially arranged swirl ports and gets a rotational motion inside the swirl chamber, Fig.3.6. The centrifugal motion of the liquid forms a hollow air core.

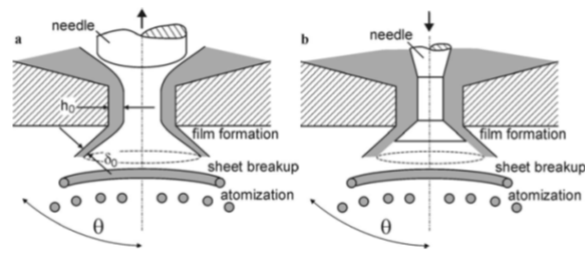


Figure 3.5: a Inwardly opening pressure-swirl atomizer, b outwardly opening nozzle

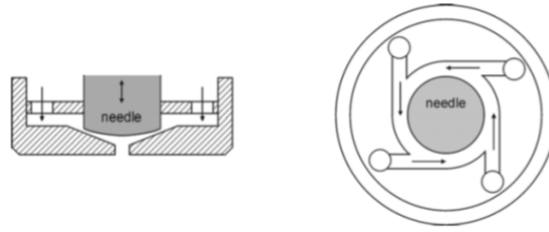


Figure 3.6: Schematic illustration of the tangentially arranged swirl ports

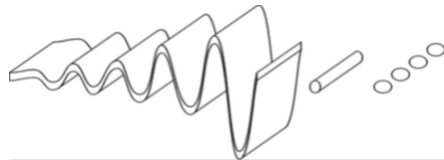


Figure 3.7: Break-up of the liquid sheet into ligaments and droplets

In the near spray region, the transition from the injector flow to the fully developed spray is modeled as a three-step mechanism, see Fig3.7. , consisting of film formation, sheet break-up, and, finally, disintegration into droplets.



## 3.2 Secondary Break-Up

### 3.2.1 Taylor-Analogy Break-Up Model

The Taylor Analogy Break-up model (TAB model), which was proposed by ORourke and Amsden [23], is based on an analogy between a forced oscillating spring-mass system and an oscillating drop that penetrates into a gaseous atmosphere with a relative velocity  $u_{rel}$ , see Fig.3.8. The force  $F$  initiating the oscillation of the mass  $m$  corresponds to the aerodynamic forces deforming the droplet and thus making its mass oscillate. The restoring force  $F_{spring} = kx$  is analogous to the surface tension force, which tries to keep the drop spherical and to minimize its deformation. The damping force  $F_{damping} = d\dot{x}$  corresponds with the friction forces inside the droplet due to the dynamic

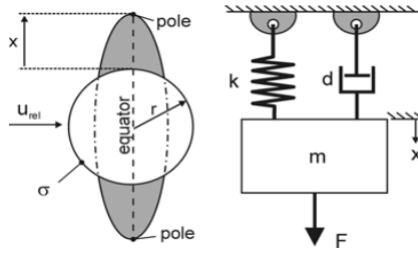


Figure 3.8: Taylor-Analogy break-up model

viscosity  $\mu_l$  of the liquid. The second order differential equation of motion for the damped spring-mass-system is

$$\ddot{x} = \frac{F}{m} - \frac{k}{m}x - \frac{d}{m}\dot{x} \quad (3.8)$$

and  $x$  is the displacement of the droplets equator from its equilibrium position, see Fig.3.8.

### 3.2.2 Kelvin-Helmholtz Break-Up Model

The Kelvin-Helmholtz model (KH model) was proposed by Reitz [22]. The model is based on a first order linear analysis of a Kelvin-Helmholtz instability growing on the surface of a cylindrical liquid jet with initial diameter  $r_0$  that is penetrating into a stationary incompressible gas with a relative velocity  $u_{rel}$ . Both the liquid and the gas are assumed to be incompressible, and the gas is assumed to be inviscid. Furthermore, it is assumed that due to the turbulence generated inside the nozzle hole the jet surface is covered with a spectrum of sinusoidal surface waves with an infinitesimal axisymmetric displacement  $\eta = \eta_0 e^{\omega t}$  ( $\eta \ll r$ ) causing small axisymmetric fluctuating pressures as well as axial and radial velocity components in both liquid and gas. These surface waves grow because of aerodynamic forces due to the relative velocity between liquid and gas (shear flow waves),

Fig.3.9.

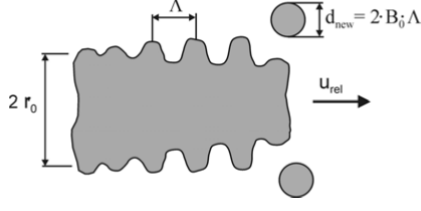


Figure 3.9: illustration of the Kelvin-Helmholtz model

The motion of liquid and gas are described by the linearized Navier-Stokes equations for both phases. The solution is found by transforming the equations of motion into stream and potential functions. The analysis, which is described in detail in Reitz and Bracco [17], yields a dispersion equation relating the growth rate  $\omega$  ( increase of amplitude per unit time) of a perturbation to its wavelength:  $\lambda = \frac{2\pi}{k}$

where  $I_0$  and  $I_1$  are modified Bessel functions of the first kind,  $K_0$  and  $K_1$  are modified Bessel functions of the second kind,  $\lambda = \frac{2\pi}{k}$  is the wave number,  $\sigma$  is the surface tension,  $l^2 = k^2 + \frac{\omega}{\nu_1}$ ,  $\nu_1 = \frac{\mu_l}{\rho_l}$  (kinematic viscosity), and the prime indicates differentiation. The numerical solution of the dispersion function shows that there is a single maximum in the wave growth rate curve  $\omega = \omega(k)$ . It is assumed that the wave with the highest growth rate  $\omega = \Omega$  will finally be sheared off the jet and form new droplets. Curve fits were generated from the numerical solutions to Eq. 3.9 for the growth rate  $\Omega$  of the fastest growing and thus most unstable surface wave,

$$\Omega \left[ \frac{\rho_l r_0^3}{\sigma} \right]^{0.5} = \frac{0.34 + 0.38.We^{1.5g}}{(1 + Z)(1 + 1.4.T^{0.6})} \quad (3.9)$$

and the corresponding wavelength

$$\frac{\Lambda}{r_0} = 9.02 \frac{(1 + 0.45.Z^{0.5})(1 + 0.4.T^{0.7})}{(1 + 0.865.We_g^{1.67})^{0.6}} \quad (3.10)$$

$$Z = \frac{\sqrt{We_l}}{Re_l}, T = Z \sqrt{We_g}, We_g = \frac{\rho_g r_0 u_{rel}^2}{\sigma}, We_l = \frac{\rho_l r_0 u_{rel}^2}{\nu_l}$$

Z and T are the Ohnesorge number and the Taylor number, and  $r_0$  is the radius of the undisturbed jet. These curve fits are shown in. Reitz [22] applied this theory to the break-up modeling of liquid droplets with radius r. Again, waves grow on the drop surface with growth rate  $\Omega$  and wavelength  $\Lambda$ . Because the new child drops are formed from the surface waves that are sheared off the parent

drops, it is assumed that the size of the new droplets is proportional to the wavelength ,

$$r = B_0 \Lambda \quad (3.11)$$

where  $B_0 = 0.61$  is a constant, the value of which is fixed. A new parcel containing product drops of size  $r_{new}$  is created and added to the computations. In contrast to the TAB model, the parent drop does not perform a complete break-up, but continuously loses mass while penetrating into the gas. This results in a shrinking radius whose rate of reduction at a certain time  $t$  depends on the difference between the actual value of droplet radius  $r$  and an equilibrium droplet size (which is equal to the child droplet radius  $r_{new}$ ) as well as on the value of a characteristic time span  $\tau_{bu}$  , (Reitz [22])

Furthermore, the rate of change of droplet radius in the parent parcel is given by

$$\frac{da}{dt} = -\frac{(a - r)}{\tau}, r \leq a \quad (3.12)$$

where the breakup time,  $\tau$  , is given by

$$\tau = \frac{3.726 B_1 a}{\Lambda \Omega} \quad (3.13)$$

and  $\Lambda$  and  $\Omega$  are obtained from Equations 3.9 and 3.10, respectively. Values of  $B_1$  can range between 1 and 60, depending on the injector characterization.

### 3.2.3 Rayleigh-Taylor Break-Up Model

The Rayleigh-Taylor model (RT model) is based on the theoretical work of Taylor[?], who investigated the instability of the interface between two fluids of different densities in the case of an acceleration (or deceleration) normal to this interface. If the two fluids are liquid and gas, the interface is stable when the acceleration is directed into the liquid, and instable disturbances can grow if the acceleration is directed into the gas. Regarding droplet and gas moving with

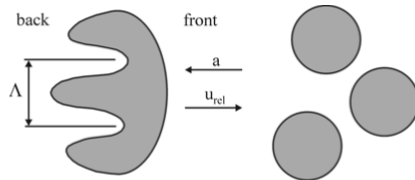


Figure 3.10: Rayleigh-Taylor instability on a liquid droplet

velocity  $u_{rel}$  relative to each other, the deceleration of the drop (in the forward direction) due to drag forces can also be treated as an acceleration of the drop in the direction of the airflow (backward direction). Thus, instable waves can grow on the back side of the drop, see Fig.3.10. The disintegration of the drop is induced by the inertia of the liquid if drops and ligaments leaving the nozzle with high velocities are strongly decelerated by the aerodynamic drag force.

$$F_{aero} = \pi r^2 C_D \frac{\rho_g u_{rel}^2}{2} \quad (3.14)$$

Dividing the drag force by the mass of the drop, the acceleration of the interface can be found,

$$a = \frac{3}{8} C_D \frac{\rho_g u_{rel}^2}{\rho_l r} \quad (3.15)$$

where  $C_D$  is the drag coefficient of the drop. Using a linear stability analysis and neglecting liquid viscosity the growth rate  $\Omega$  and the corresponding wavelength  $\Lambda$  of the fastest growing wave are

$$\Omega = \sqrt{\frac{2}{3\sqrt{3}\sigma} \frac{[a(\rho_l - \rho_g)]^{\frac{3}{2}}}{\rho_l + \rho_g}} \quad (3.16)$$

and

$$\Lambda = C_3 2\pi \sqrt{\frac{3\sigma}{a(\rho_l - \rho_g)}} \quad (3.17)$$

# Chapter 4

## CFD Spray Model

### 4.1 Numerical Simulation

#### 4.1.1 Transport Equations

The simulation software (Fluent) solves a number of transport equations depending on the user's specific problem setup. In this section an overview is given of the (general) continuity, momentum, energy, species and turbulence equations [24]. Additional models and settings that are required to deal with sprays are treated in the next sections.

**Continuity equation:**The general continuity equation is written as follows:

$$\frac{\partial \rho}{\partial t} + \nabla \cdot (\rho \vec{v}) = S_m = f(x, v, r, T_d; t) = \int \int \int_{vol} \rho_l 4\pi r^2 R f dr dv dT_d \quad (4.1)$$

$$R = \frac{\partial r}{\partial t};$$

$$\frac{dx}{dt} = v;$$

$$\frac{v}{t} = F;$$

$$\frac{dr}{dt} = R$$

where  $S_m$  is a mass source from the discrete phase due to evaporation of droplets. It can also be a user-defined mass source.

**Momentum equations** :The momentum equation that is solved in this study is:

$$\frac{\partial}{\partial t}(\rho \vec{v}) + \nabla \cdot (\rho \vec{v} \vec{v}) = -\vec{\nabla} p + \vec{\nabla} \cdot \vec{\tau} + \vec{F} \quad (4.2)$$

Here  $p$  is the static pressure,  $\vec{\tau}$  is the stress tensor and  $\vec{F}$  is a body force due to interaction of the discrete phase with the continuous phase and/or a user-defined momentum source. The gravity term in the momentum equation is neglected because of the minimal contribution compared to the high momentum injection event.

**Energy equation:** The energy equation in Fluent is written as follows:

$$\frac{\partial}{\partial t}(\rho E) + \vec{\nabla} \cdot [\vec{v}(\rho E + p)] = \vec{\nabla} \cdot [(k + k_t)\vec{\nabla} T - \sum_j h_j \vec{J}_j + (\vec{\tau} \cdot \vec{v})] + S_e \quad (4.3)$$

where the term between the brackets on the right hand side consists of energy transfer due to conduction, species diffusion and viscous dissipation, respectively.  $S_e$  is a user-defined energy source. Energy  $E$  is defined as follows:

$$E = h - \frac{p}{\rho} + \frac{\vec{v} \cdot \vec{v}}{2} \quad (4.4)$$

Here in  $h$  is the enthalpy for ideal gases, and is written as a summation of mass fractions times species enthalpy:

$$h = \sum_j Y_j h_j \quad (4.5)$$

It is important, to state that the enthalpy is calculated by integrating the specific heat from  $T_{ref}$  to the instantaneous temperature  $T$ , whereby the reference temperature in Fluent is  $298.15K$ :

$$h_j = \int_{T_{ref}}^T C_{p,j} dT, T_{ref} = 298.15K \quad (4.6)$$

**Species transport equations** In spray simulations there are at least two different species, one species is in the gas phase (oxidizer) and an other one is injected (fuel), which after evaporation goes into the gas phase where it can mix with the oxidizer.  $N - 1$  transport equations for  $N$  species are solved because the sum of fractions must equal one. The transport equation for the  $i^{th}$  species is as follows:

$$\frac{\partial}{\partial t}(\rho Y_i) + \vec{\nabla} \cdot (\rho \vec{v} Y_i) = -\vec{\nabla} \cdot \vec{J}_i + S_i \quad (4.7)$$

$S_i$  is again a source from the liquid droplet phase that is activated when evaporation occurs. Also userdefined sources are included in this term. Species transport due to diffusion is calculated via the diffusion flux  $J_i$ . For turbulent flows this flux is:

$$\vec{J}_i = -(\rho D_{i,m} + \frac{\mu_t}{Sc_t}) \vec{\nabla} Y_i \quad (4.8)$$

where  $D_{i,m}$  is the diffusion coefficient of the  $i^{th}$  species in the mixture.  $\mu_t$  is the turbulent dynamic viscosity and  $Sc_t$  is the turbulent Schmidt number:

$$Sc_t = \frac{\mu_t}{\rho D_t} \quad (4.9)$$

which is equal to 0.7 by default.  $D_t$  is the turbulent diffusivity.

**Turbulence equations** Turbulence is dealt with the transport equations for the turbulent kinetic energy  $k$  and its dissipation rate  $\epsilon$ . Here the realizable  $k - \epsilon$  model is preferred because it is more suitable for axisymmetric jets than the standard one [24].

$$\frac{\partial}{\partial t}(\rho k) + \vec{\nabla} \cdot (\rho k \vec{v}) = \vec{\nabla} \cdot [(\mu + \frac{\mu_t}{\sigma_k}) \vec{\nabla} k] + \mu_t S^2 - \rho \epsilon \quad (4.10)$$

$$\frac{\partial}{\partial t}(\rho \epsilon) + \vec{\nabla} \cdot (\rho \epsilon \vec{v}) = \vec{\nabla} \cdot [(\mu + \frac{\mu_t}{\sigma_\epsilon}) \vec{\nabla} \epsilon] + \rho C_1 S \epsilon - \rho C_2 \frac{\epsilon^2}{k + \sqrt{v \epsilon}} \quad (4.11)$$

#### 4.1.2 Euler- Lagrangian Model(Discrete Phase Model in Fluent terms)

Fluent provides a model that is specially developed for spray simulations, or more general suspended particle trajectory simulations. This is the Discrete Phase Model (DPM) and it is based on the so-called Euler-Lagrange method. In the computational domain there are two separate phases present, namely the continuous and the discrete phase (particles). The transport equations from the previous section are solved for the continuous phase only and the motion of particles is dealt with particle trajectory calculations. Through an iterative solution procedure the mass, momentum and energy interaction between both phases can be realized. Some important aspects of the DPM model are presented in this section.

**Atomizer** In order to simulate spray formation, (discrete) liquid particles have to be introduced to interact with the present (continuous) gas phase. As described in Chapter 2, in Gasoline sprays the primary breakup takes place in the atomization regime. So, it is assumed that there is no liquid core; all the liquid is formed into droplets immediately after the exit of the nozzle hole. That is

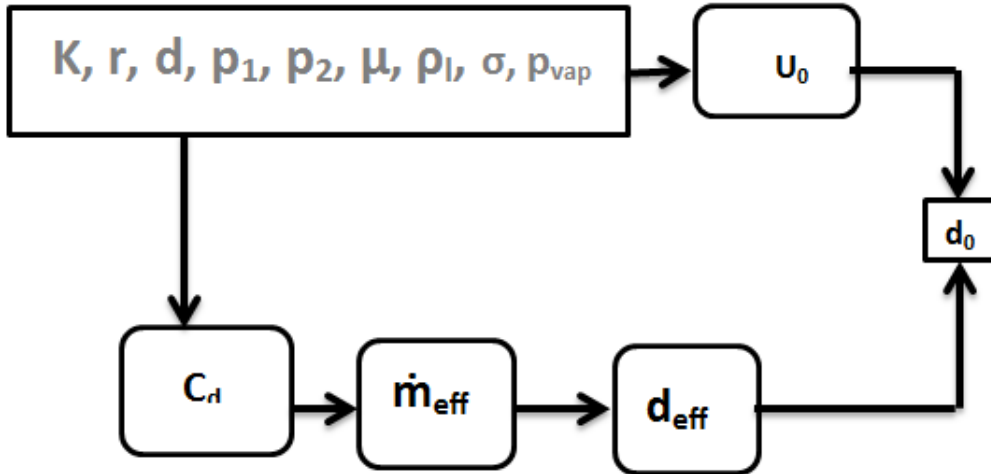


Figure 4.1: Atomizer scheme; the way initial velocity and diameter are calculated

where the so-called atomizer model comes into play. The atomizer creates initial conditions, that depend on the internal nozzle flow, for further particle trajectory calculations by defining initial droplet diameter, velocity and the cone angle of the spray. Here the procedure to determine the internal nozzle flow state and its consequence for the calculation of initial quantities is presented without going into the details.

In Fluent's Plain-Orifice Atomizer Model three kinds of internal nozzle flows are defined, namely single-phase, cavitating and flipped flows. Fig 4.1 shows schematic cross-section drawings of those possible nozzle flows. The upstream radius  $r$ , hole diameter  $d$  and length  $L$  of the nozzle are geometrical details that are used as parameters in empirical relations. On the righthand side also the corresponding criteria based on the cavitation number  $K$  (see Figure 4.1) are given.  $K_{incept}$  and  $K_{crit}$  are the cavitation number at which inception occurs and the critical cavitation number, respectively. These cavitation numbers can be obtained with empirical relations based on experimental data. Cavitating nozzle flow is the main regime that occurs in today's high pressure Gasoline injectors.

Once the internal flow state of the nozzle is known, the calculation of the initial droplet diameter and velocity for the cavitating case proceeds according to the scheme in Figure 4.2. Given the predetermined cavitation number, the case data ( $r$ ,  $d$ ,  $p_1$  and  $p_2$ ; see Fig 4.2 for definitions), and material properties in the upper left frame, the discharge coefficient  $C_d$  and the initial velocity  $u_0$  are calculated. Then, via the effective mass flow rate  $m_{eff}$  and the effective nozzle diameter  $d_{eff}$



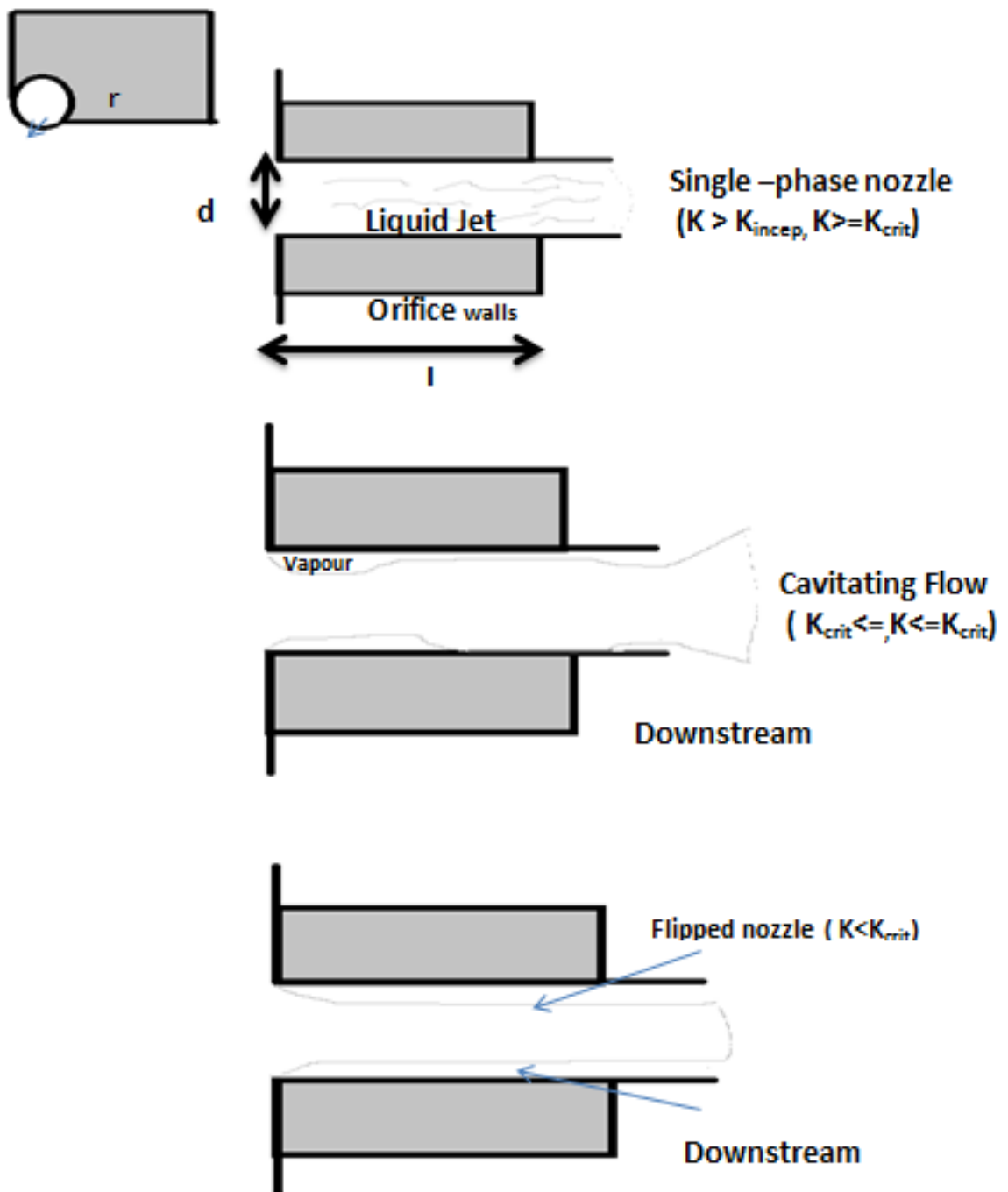


Figure 4.2: Plain-Orifice Atomizer, possible nozzle flows with cavitation number criteria [24]

an initial droplet diameter is obtained.

To complete the initialization of the droplets, apart of the size and velocity, the initial direction (cone angle) should be defined. This is again done by an empirical relation, but now for the cone angle. The cone angle, from now on also-called spray angle, is twice the angle between the outer boundary of the spray and the main spray axis. In literature there are several spray angle relations proposed but the relation proposed by(Reitz [3]) which

$$\tan\left(\frac{\theta}{2}\right) = \frac{2\pi}{3C_A} \sqrt{\frac{3\rho_a}{\rho_f}} \quad (4.12)$$

$$C_A = 3 + \frac{L}{3.6d}$$

seems complete because it takes into account fluid property as well as nozzle geometry information. However, later on it will be clear that also other relations with similar appearances give rather different results.

**Particle motion** The trajectory calculation of a discrete phase particle is done by integrating the force balance on the droplet. The force balance in vector notation is written as follows:

$$\frac{d\vec{v}_p}{dt} = F_D(\vec{v} - \vec{v}_p) + \frac{\rho_p - \rho}{\rho_p} \vec{g} + \frac{\rho}{\rho_p} \vec{v}_p \cdot (\vec{\nabla} \vec{v}) \quad (4.13)$$

where the left hand term is the acceleration of the particle in question, the term with  $F_D$  is the drag force on the particle.  $F_D$  is defined as:

$$F_D = \frac{18\mu}{\rho_p d_p^2} \frac{C_D Re}{24} \quad (4.14)$$

The drag coefficient  $C_D$  is determined from the dynamic drag model that accounts for the effects of droplet distortion, linearly varying the drag between that of a sphere and a disk [24]. The term with  $\vec{g}$  in force balance equation (4.12) is the contribution of the gravitational acceleration. In this study the gravitational effect is neglected because of the very low mass of the droplets and the short injection times. The last term is an additional force that arises due to pressure gradients in the fluid. However this contribution is accounted for, in case of a relative large constant volume pressure cell, gradients of pressure are not that large, in particular when non-reacting sprays are concerned.

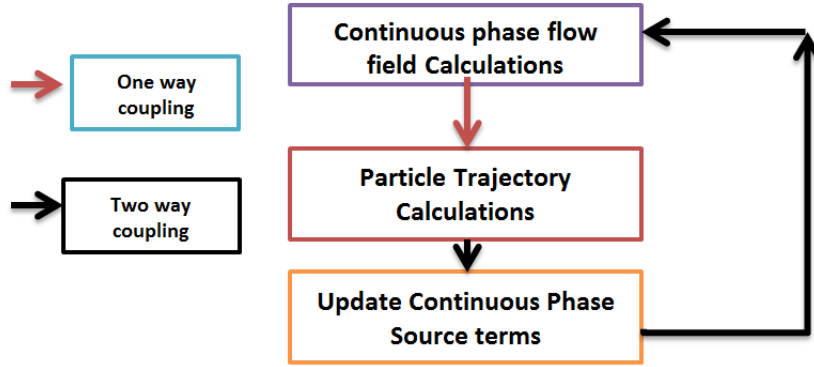


Figure 4.3: Solving procedure for one-way and two-way coupling

## 4.2 Phase coupling

While the discrete particle phase is always influenced by the continuous phase solution (one-way coupling), the other way around (two-way coupling) is just provided as an option. In the one-way coupling case the continuous phase is solved first thereafter the particle trajectory calculation is performed. When two-way coupling is applied an iterative procedure is followed. Then, after the particle trajectory calculation the continuous flow field is solved again with updated source terms until convergence is reached. See Fig 4.3 for a graphical representation of the procedure. Because the discrete phase during an injection event possesses high momentum, thus affects the continuous phase considerably, the two-way coupling is turned on.

Several heat and mass transfer relationships, termed laws, are available in ANSYS FLUENT and the physical models employed in these laws are described in this section.

The laws that to be activated depend upon the particle type that we select which is shown in Table4.1 below.

As we know our attention is the study of mixture strategies before combustion. So the droplet model was activated in turn the corresponding laws also gets activated.

Therefore, it is very important to know the theory behind the coupling process with many species. The following section deals with the laws of Heat and Mass transfer when a particle moves for an integral timestep.

Table 4.1: Laws activated based on select of droplet type

Particle Type	Description	Laws Activated
Massless		
Inert	inert/heating or cooling	1, 6
Droplet	heating/ evaporation / boiling	1, 2, 3, 6
Combusting	heating; evolution of volatiles/swelling; heterogeneous surface reaction	1, 4, 5, 6
Multicomponent	multicomponent droplets/particles	7

### Inert Heating or Cooling (Law 1/Law 6)

The inert heating or cooling laws (Laws 1 and 2) are applied when the particle temperature is less than the vaporization temperature that we define,  $T_{vap}$ , and after the volatile fraction,  $f_{v,0}$ , of a particle has been consumed. These conditions may be written as Law 1:

$$T_P < T_{vap} \quad (4.15)$$

Law 6:

$$m_p \leq (1 - f_{v,0})m_{p,0} \quad (4.16)$$

where  $T_p$  is the particle temperature,  $m_{p,0}$  is the initial mass of the particle, and  $m_p$  is its current mass.

Law 1 is applied until the temperature of the particle/droplet reaches the vaporization temperature. At this point a noninert particle/droplet may proceed to obey one of the mass-transfer laws (2, 3, 4, and/or 5), returning to Law 6 when the volatile portion of the particle/droplet has been consumed. (Note that the vaporization temperature,  $T_{vap}$ , is an arbitrary modeling constant used to define the onset of the vaporization/ boiling/volatilization laws.)

When using Law 1 or Law 6, we use a simple heat balance to relate the particle temperature,  $T_p(t)$ , to the convective heat transfer and the absorption/emission of radiation at the particle surface is neglected:

$$m_p c_p \frac{dT_p}{dt} = h A_p (T_\infty - T_p) + \text{Radiation effects} \quad (4.17)$$

where

$m_p$  = mass of the particle (kg)  $c_p$  = heat capacity of the particle (J/kg-K)  $A_p$  = surface area of the particle ( $m^2$ )  $T_\infty$  = local temperature of the continuous phase (K)  $h$  = convective heat transfer coefficient ( $W/m^2-K$ )

Equation 4.17 assumes that there is negligible internal resistance to heat transfer, i.e., the particle is at uniform temperature throughout.

Radiation heat transfer to the particle is neglected in our present study.

Equation 4.17 is integrated in time using an approximate, linearized form that assumes that the particle temperature changes slowly from one time value to the next.

As the particle trajectory is computed, the integration of Equation 4.17 is done to obtain the particle temperature at the next time value.

where  $\Delta t$  is the integration timestep

The heat transfer coefficient,  $h$ , is evaluated using the correlation of Ranz and Marshall [27]:

$$Nu = \frac{h d_p}{k_\infty} = 2.0 + 0.6 Re_d^{\frac{1}{2}} Pr^{\frac{1}{3}} \quad (4.18)$$

where

$d_p$  = particle diameter (m)  $k_1$  = thermal conductivity of the continuous phase (W/m-K)  $Re_d$  = Reynolds number based on the particle diameter and the relative velocity  $Pr$  = Prandtl number of the continuous phase ( $\frac{c_p \sigma}{k_\infty}$ )

Finally, the heat lost or gained by the particle as it traverses each computational cell appears as a source or sink of heat in subsequent calculations of the continuous phase energy equation. During Laws 1 and 6, particles/droplets do not exchange mass with the continuous phase and do not par-

ticipate in any chemical reaction.

**Droplet Vaporization (Law 2)** Law 2 is applied to predict the vaporization from a discrete phase droplet. Law 2 is initiated when the temperature of the droplet reaches the vaporization temperature,  $T_{vap}$ , and continues until the droplet reaches the boiling point,  $T_{bp}$ , or until the droplets volatile fraction is completely consumed:

$$T_{vap} \leq T_p < T_{bp} \quad (4.19)$$

$$m_p \geq (1 - f_{v,0})m_{p,0} \quad (4.20)$$

### Mass Transfer During Law 2

During Law 2, the rate of vaporization is governed by gradient diffusion, with the flux of droplet vapor into the gas phase related to the difference in vapor concentration at the droplet surface and the bulk gas:

$$N_i = k_c(C_{i,s} - C_{i,\infty}) \quad (4.21)$$

where  $N_i$  = molar flux of vapor ( $\text{kgmol}/m^2 - s$ )

$k_c$  = mass transfer coefficient (m/s)

$C_{i,s}$  = vapor concentration at the droplet surface ( $\text{kgmol}/m^3$ )

$C_{i,\infty}$  = vapor concentration in the bulk gas ( $\text{kgmol}/m^3$ )

The concentration of vapor at the droplet surface is evaluated by assuming that the partial pressure of vapor at the interface is equal to the saturated vapor pressure,  $p_{sat}$ , at the particle droplet temperature,  $T_p$ :

$$C_{i,e} = \frac{P_{sat}(T_p)}{RT_p} \quad (4.22)$$

where R is the universal gas constant.

The concentration of vapor in the bulk gas is known from solution of the transport equation for species i for nonpremixed or partially premixed combustion calculations:

$$C_{i,\infty} = X_i \frac{P}{RT_\infty} \quad (4.23)$$

where  $X_i$  is the local bulk mole fraction of species i,  $p$  is the local absolute pressure, and  $T_\infty$  is the local bulk temperature in the gas.

The mass transfer coefficient in Equation 4.21 is calculated from the Sherwood number correlation[27]

$$Sh_{AB} = \frac{k_c d_p}{D_{i,m}} = 2.0 + 0.6 Re_d^{\frac{1}{2}} Sc^{\frac{1}{3}} \quad (4.24)$$

where

$D_{i,m}$  = diffusion coefficient of vapor in the bulk ( $m^2/s$ )  $Sc$  = the Schmidt number,  $\frac{\mu}{\rho D_{i,m}}$   $d_p$  = particle (droplet) diameter (m)

The vapor flux given by Equation 4.21 becomes a source of species i in the gas phase species transport equation

The mass of the droplet is reduced according to

$$m_p(t + \Delta t) = m_p(t) - N_i A_p M_{w,i} \Delta t \quad (4.25)$$

where  $M_{w,i}$  = molecular weight of species i (kg/kgmol)  $m_p$  = mass of the droplet (kg)  $A_p$  = surface area of the droplet ( $m^2$ )

**Heat Transfer to the Droplet** Finally, the droplet temperature is updated according to a heat balance that relates the sensible heat change in the droplet to the convective and latent heat transfer between the droplet and the continuous phase:

$$m_p c_p \frac{dT_p}{dt} = h A_p (T_\infty - T_p) + \frac{dm_p}{dt} h_{fg} + \text{Radiation effect} \quad (4.26)$$

$c_p$  = droplet heat capacity (J/kg-K)

$T_p$  = droplet temperature (K)

$h$  = convective heat transfer coefficient (W/m<sup>2</sup>-K)

$T_1$  = temperature of continuous phase (K)

$\frac{dm_p}{dt}$  = rate of evaporation (kg/s)  $h_{fg}$  = latent heat (J/kg)

The heat transferred to or from the gas phase becomes a source/sink of energy during subsequent calculations of the continuous phase energy equation.

**Droplet Boiling (Law 3)** Law 3 is applied to predict the convective boiling of a discrete phase

droplet when the temperature of the droplet has reached the boiling temperature,  $T_{bp}$ , and while the mass of the droplet exceeds the nonvolatile fraction,  $(1f_{v,0})$ :

$$T_p \geq T_{bp} \quad (4.27)$$

$$m_p > (1 - f_{v,0})m_{p,0} \quad (4.28)$$

When the droplet temperature reaches the boiling point, a boiling rate equation is applied [27]:

$$\frac{d(d_p)}{dt} = \frac{4k_\infty}{\rho_p c_{p,\infty} d_p} (1 + 0.23\sqrt{Re_d}) \ln \left[ 1 + \frac{c_{p,\infty}(T_\infty - T_p)}{h_{fg}} \right] \quad (4.29)$$

where  $c_{p,\infty}$  = heat capacity of the gas (J/kg-K)

$\rho_p$  = droplet density (kg/m<sup>3</sup>)

$k_\infty$  = thermal conductivity of the gas (W/m-K)

Equation 4.29 was derived assuming steady flow at constant pressure.

Note that the model requires  $T_1 > T_{bp}$  in order for boiling to occur and that the droplet remains at fixed temperature ( $T_{bp}$ ) throughout the boiling law.

The droplet is assumed to stay at constant temperature while the boiling rate is applied. Once the boiling law is entered it is applied for the duration of the particle trajectory. The energy required for vaporization appears as a (negative) source term in the energy equation for the gas phase. The evaporated liquid enters the gas phase as species *i*, as defined by your input for the destination species

### Source terms

1. The exchange of mass, momentum and energy between the continuous and discrete phases is computed by the change of the concerning quantity as a particle passes through a computational cell, see Fig 4.4. These changes act as sources in the continuous flow calculation.
2. So in case of a non-reacting spray in a hot environment, the mass and momentum sources are positive. But the energy source is usually negative (energy sink) because the fuel with a relative low pre-injection temperature has to be heated and possibly evaporated.



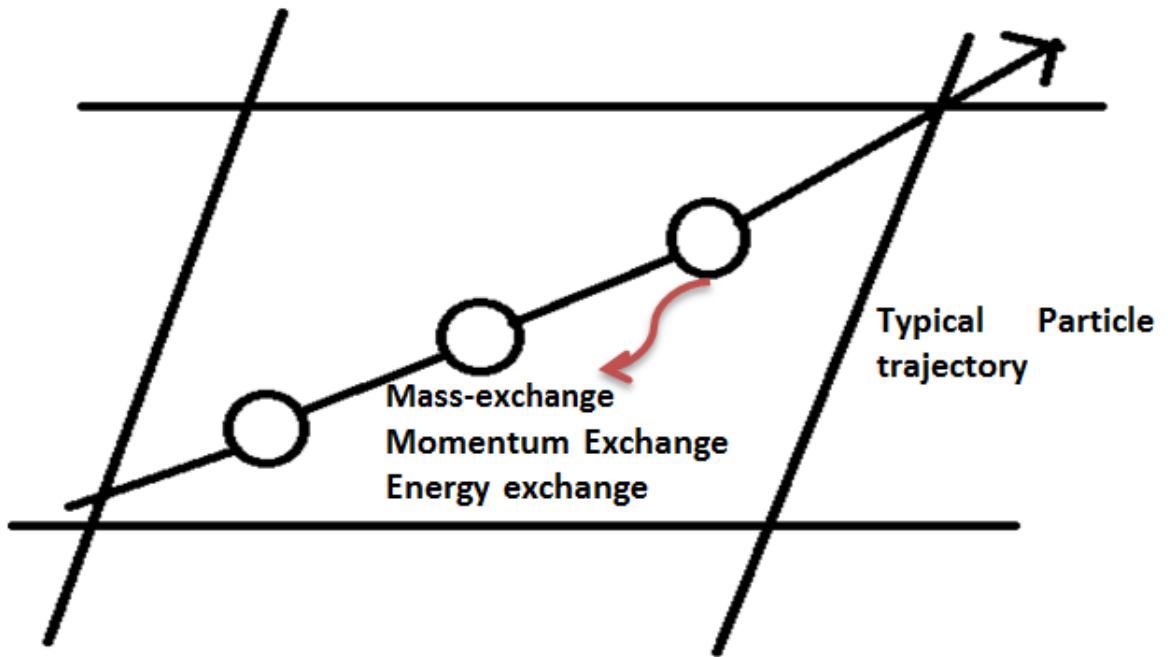


Figure 4.4: Discrete phase particle traveling through a continuous phase cell, exchanging mass, momentum and energy [24]

3. For non-reacting droplets Fluent makes a distinction between three modes of heating/vaporization. The first one is heating without vaporization until the user-defined vaporization temperature is defined. From then, the droplets can heat up and vaporize at the same time.
4. The vaporization temperature is of course an artificial boundary between heating only and vaporization, because liquid can vaporize at any temperature, hence the concept of vapor pressure. But in this way the mass exchange calculation due to vaporization at low temperatures can be neglected to save time. Finally, when the user-defined boiling temperature is reached all added heat to the particles is used for vaporization, so the droplet temperature does not change any more (shown in Fig 4.5)

**Limitations** So far the DPM model of Fluent seems to contain all necessary modeling features to capture most of the spray physics present in Gasoline injection systems, but there are also some major shortcomings from a computational point of view. Apart from issues that are described in the next sections, probably the most important drawback of the DPM model arises from the Euler-Lagrange approach assumption that at most 10 to 12 volume percent of a cell should contain discrete phase particles. Otherwise the discrete phase would occupy a significant amount of the continuous

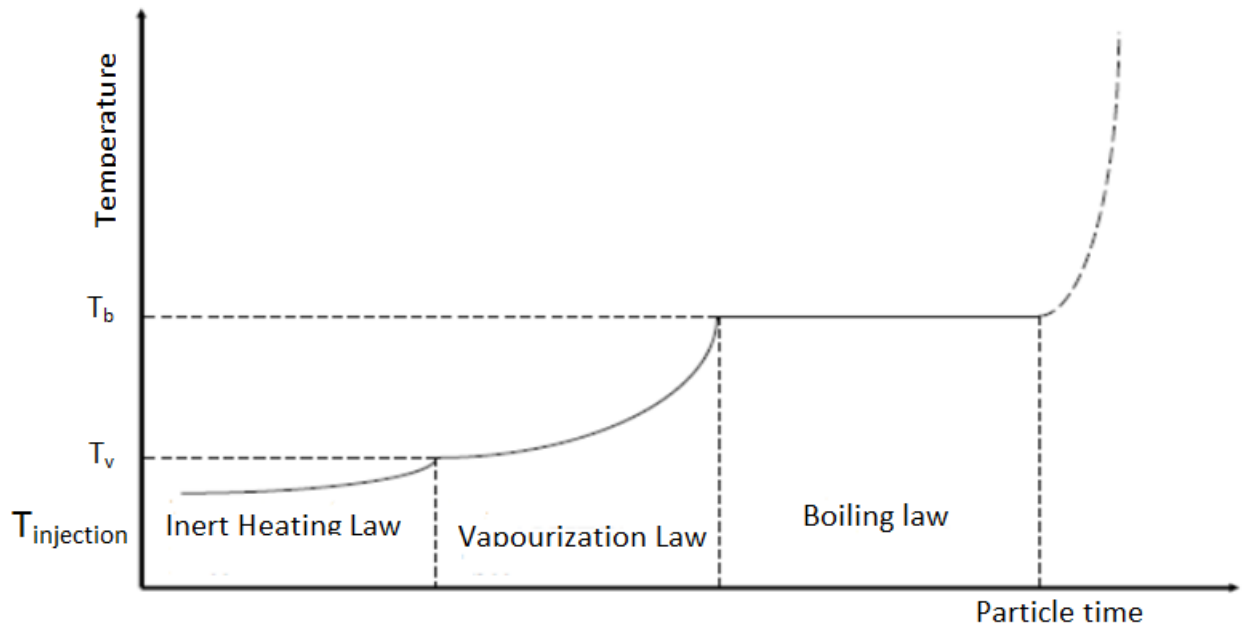


Figure 4.5: Change in phase of the droplet with particle time[24]

phase volume, whereas in the continuous phase calculation the volume is constant and equal to that of the user-specified size. This would give erroneous interaction sources between the two phases. In practice this restriction means that computational cells, especially near the nozzle exit, must be big enough. This is the point where a tradeious have to be made between relative large cells in favor of the DPM model on one hand, and small cells to solve the high velocity flow field as accurate as possible on the other hand. A direct consequence of large cells is the cell shape and orientation dependency of the results .

Additionally, when cell sizes are decreased to improve the flow field resolution, the statistics (related to the amount of parcels) would run into convergence problems [25]. This has to do with the low number of parcels per cell, therefore the total amount of parcels should be increased, leading to a huge number of parcels and therefore also very high computing times. Despite the known limitations of the DPM model, it is worthwhile investigating to what extent these limitations restrict the reach of the ultimate goal; modeling direct injection of a reactive spray in the variable volume of an auto-ignition engine. Therefore the following sections show the applied Fluent settings and the resulting solutions.

## Model Settings

1. In the section with the results of the DPM spray model, comparisons with experimental data gained from high pressure cell setups with a constant volume are done. This approach to validate spray models is very common, because in a constant volume cell the mean pressure stays approximately constant even when combusting sprays are considered. Important features like spray angle and penetration are then relatively easy to measure due to the controlled and reproducible conditions. In this study experimental data from several research groups is used. For more information on their specific experimental layout and measuring techniques see Table 1.3

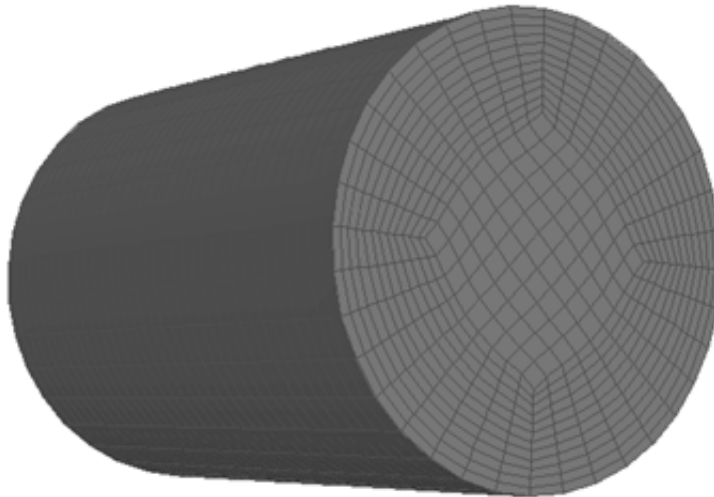


Figure 4.6: Figure showing Meshing of cylinder chamber with coarse mesh at nozzle position

2. First of all a mesh is constructed to define the constant volume environment wherein the spray is simulated. This is done with the default drawing and mesh creating tool of Fluent, named ICEMCFD shown in Fig 4.6 . Two different base meshes are created taking the model related cell size restriction into account. In typical high pressure fuel injection cases a cell size near the nozzle of  $2.5mm^3$  and  $1.0mm^3$  is common and gives the most realistic results for ILASS [5] and ICLASS[4] respectively.
3. Boundary conditions on the mesh surfaces are set as follows. All other surfaces have adiabatic constraints. There is inlet with very little velocity and one pressure outlet. The meshes do not include detailed interior geometry of the experimental constant volume apparatus. This

Table 4.2: Known values obtained from the papers for calculating unknown parameters

Given Data(Base Case)	Paper[ILASS]	Paper[ICLASS]	Units
Chamber Pressure	1.1	Atmospheric	MPa
Mass flow rate	0.00605	Vary	Kg/s
Inj Velocity	102	Vary	m/s
Simulation Software	Fluent	StarCD	N/A
Cell size	2.5	1.0	mm <sup>3</sup>
Injection Pressure	N/A	10	MPa
Initial spray angle /Cone Angle	15(7.5 Fluent)	67(33.5 Fluent)	degress
Inj period	2.5	3	ms
Type of Injector	Solid cone	Hollow cone(swirl)	N/A

Table 4.3: Data Inputs for DPM Model of Fluent

Unknown Term	Formula	Value	Units
Particle flow time step	$\Delta t = \frac{t}{\lambda} = \frac{\Delta X}{u_p \lambda}$	$10^{-5}$	seconds
No of Particles	$n = \frac{64u_{inj}}{4D}$	$5 \times 10^5$	Particles per sec
Nozzle Dia(D)	$\frac{m_{inj}}{n\rho_l \frac{\pi}{4} u_{inj}}$	0.3	mm
Spray Cone Angle	$\tan(\frac{\theta}{2}) = \frac{2\pi}{3C_A} \sqrt{\frac{3\rho_a}{\rho_f}}$	7.5	degrees

is allowed because the high pressure cells have cube or cylinder like volumes that are much bigger than the space occupied by the spray.

4. In the next section only simulation results for dodecane and iso-octane sprays are considered . By choosing a single-component fuel like dodecane , all temperature dependent material properties are defined relatively simple. The specific heat, thermal conductivity, viscosity, vapor pressure and surface tension of the liquid dodecane are defined as function of temperature. Also the specific heat of all gaseous species is set temperature dependent. All these data are gained from the thermophysical database from DIPPR[26].
5. In the DPM model two-way coupling of the phases and droplet collision and breakup are enabled. The spray origin, spray direction, initial temperature, nozzle diameter and with the modeled section corresponding mass flow are prescribed.

### Calculation of Unknown inputs to Fluent from known terms

From the literature we obtained some thermal and geometrical inputs for spray simulation to proceed. From this inputs , using analytic and empirical relations we find the unknown terms. From the Tables 4.2 and 4.3 we could understand this better.

## 4.3 Results and Parametric Dependencies

### Spray Length

Spray lengths are experimentally determined with a Laser Sheet Imaging and Phase Doppler Particle Analyzer tests. This is a line of sight technique that makes use of the deflection of light that travels through a medium with density gradients. While this is an appropriate method to measure spray lengths, it makes direct comparison with numerical results not trivial. In order to make validation possible, a numerical technique is developed. Using this technique an image is constructed with virtual rays of light that travel through the 3D density domain that is extracted from the model results. The position on the resulting image where the rays are most far from the nozzle exit is considered to mark the end of the spray in the length direction.

Table 4.4: Table describes the geometry, cell size, No of cells, operating conditions with spray generation snapshots at different particle Flow time

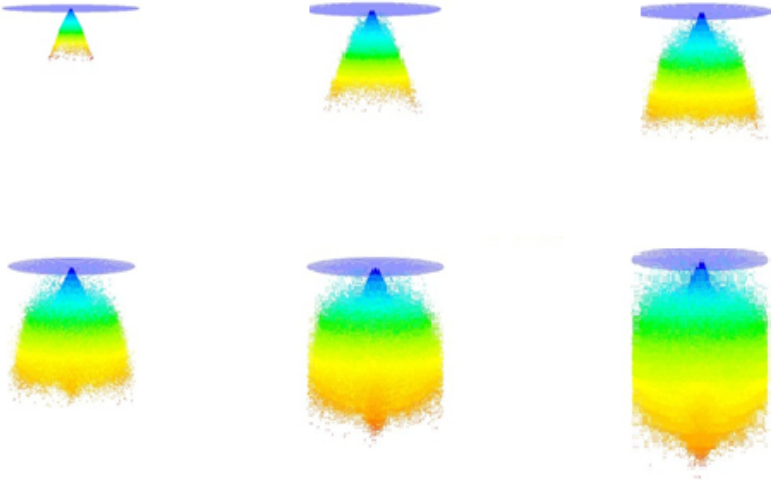
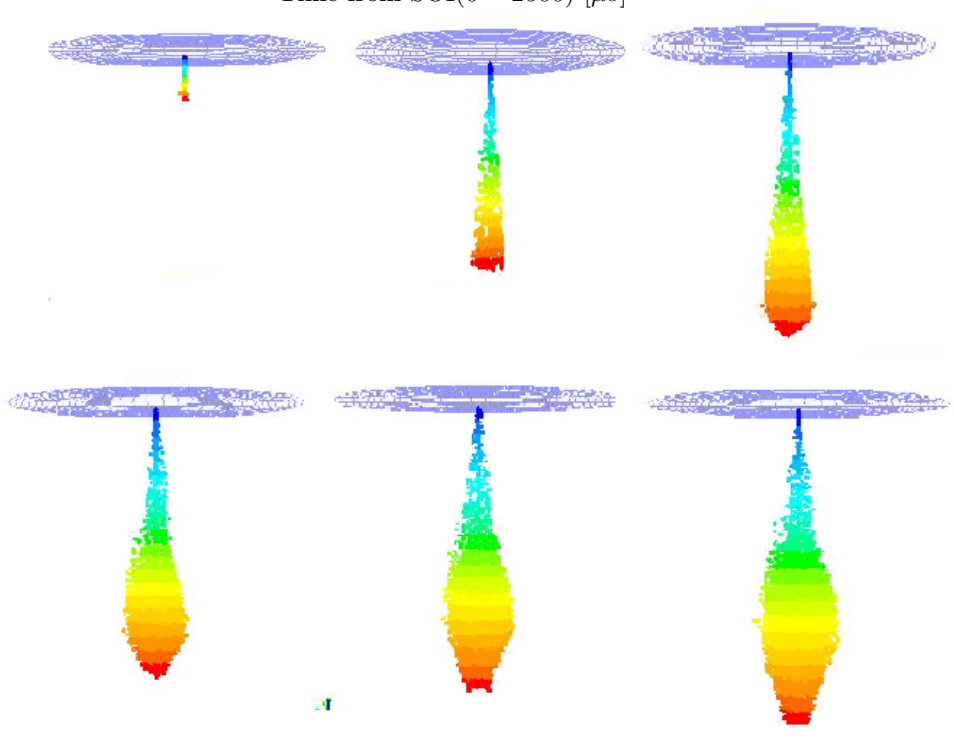
Paper	Geometry size( $L \times D$ )	Cell size	No of cells
ICLASS	Cylindrical( $90mm \times 60mm$ )	$1mm^3$	
$P_{air}$	Gasoline injection pressure $P_{inj} = 10MPa$ (Pressure Swirl Atomizer) ICLASS Paper Time from SOI(0 – 2500) [ $\mu s$ ]		
Ambient			

Table 4.5: Table describes the geometry , cell size , No of cells ,operating conditions with spray generation snapshots at different particle Flow time

Paper	Geometry size( $L \times D$ )	Cell size	No of cells
ILASS	Cylindrical( $90mm \times 60mm$ )	$2.5mm^3$	
$P_{air}$	Solid cone ILASS Paper Time from SOI(0 – 2500) [ $\mu s$ ]		
1.1MPa			

## Procedure for calculating penetration depth in simulation study

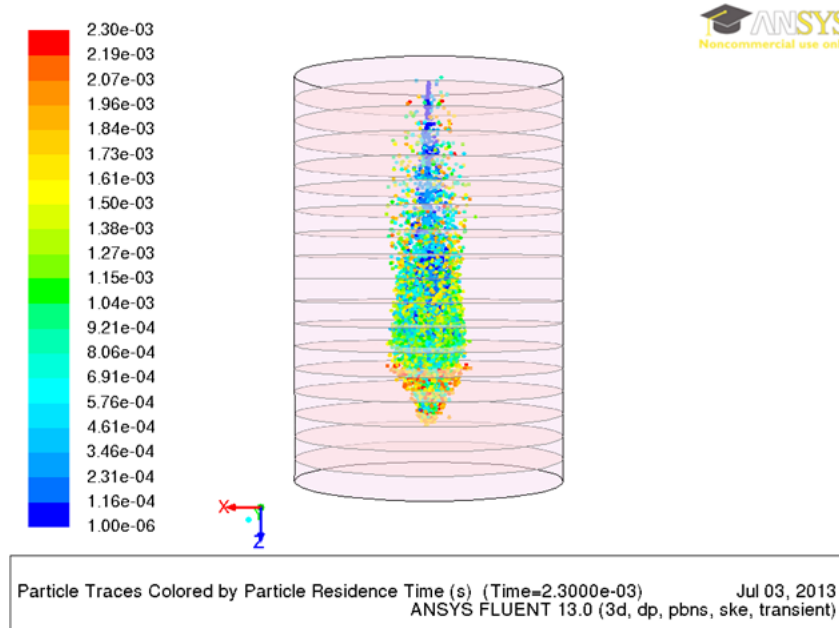


Figure 4.7: Figure showing procedure for calculating penetration depth

There are so many relations for every paper which they follow to find the spray penetration as the time advances .The one among (see [27])the relation is defined as

$$S = K \left( \frac{P_{inj} - P_a}{\rho_a} \right) \sqrt{Dt} + C \quad (4.30)$$

Where S is the spray penetration, K is an empirical constant,  $P_{inj}$  the injection pressure,  $P_a$  the ambient pressure,  $\rho_a$  the ambient density, D the injector orifice diameter, t is the time after start of injection and C is a correction time constant.

But the procedure we followed is quiet simple by monitoring volume fraction for every timestep or flow time at different planes shown in Fig 4.7 .The technique was to see at which time from the monitor data of volume fraction reaches a minimum of 0.02 on a particular plane tells the spray penetration(that is spray has reached that plane and remaining planes show zero volume fraction of fuel) .Tables 4.3 and 4.4 shows the peneration of spray with time at particular operating conditions for a GDI injector.

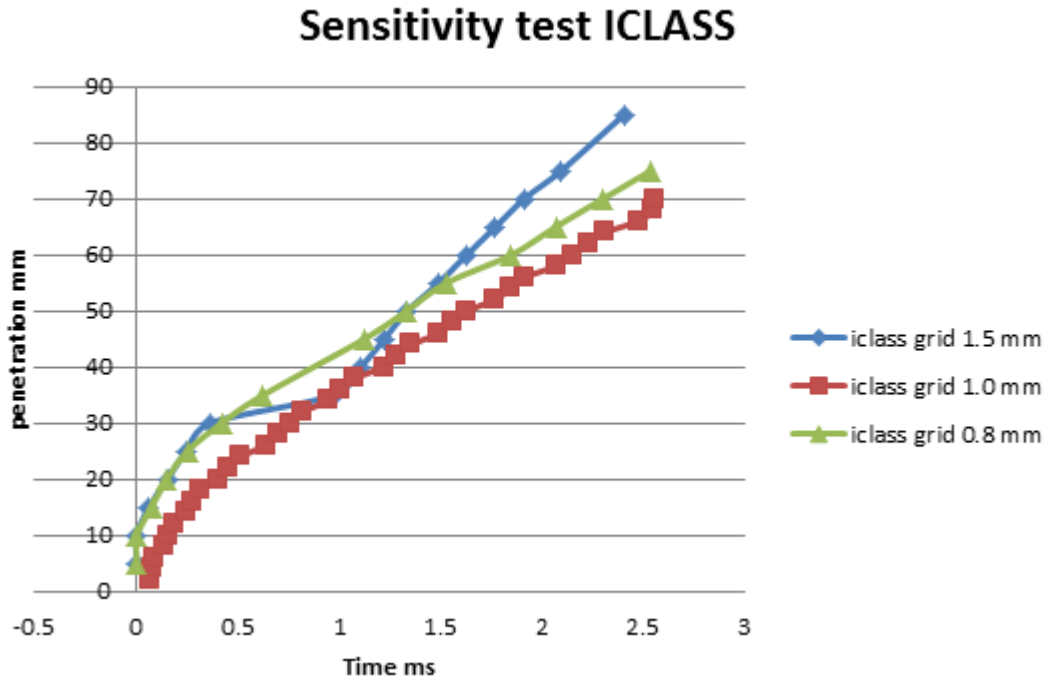


Figure 4.8: Grid sensitivity test for ICLASS

### Mesh dependency

First, as expected, the DPM model appears to be highly dependent on cell sizes in the (square) mesh. The red solid lines are spray lengths as function of time for  $2.5mm^3$  cubic cells and the blue dotted lines are for the  $0.8mm^3$  cells and green dotted lines are for the  $1.0mm^3$  cells . The difference with the two other configurations is very large, and may be more important, they do not follow the same increasing trend.

### Solver timestep

Second, the time step of the time-dependent solver gives rise to very large differences in spray length. Decreasing the timestep to  $5 \times 10^{-6}$  s leads to little improvement while computational expenses increase tremendously. Even a smaller timestep like  $10^{-6}$  s is tried, but it gives alternately flipped and cavitating nozzle flows, and the solution does not converge at all. This is remarkable because the internal nozzle flow is determined with empirical relations that does not depend on the solver timestep, but depend on nozzle geometry and fluid properties. Anyway, even the best result ( $1mm^3$  cell and timestep of  $10^{-6}$  s) is still far off from the experimental curve for ICLASS.

and the best result ( $2.5mm^3$  cell and timestep of  $10^{-5}$  s) is found from the parametric study on timestep



### Sensitivity test on penetration depth ILASS

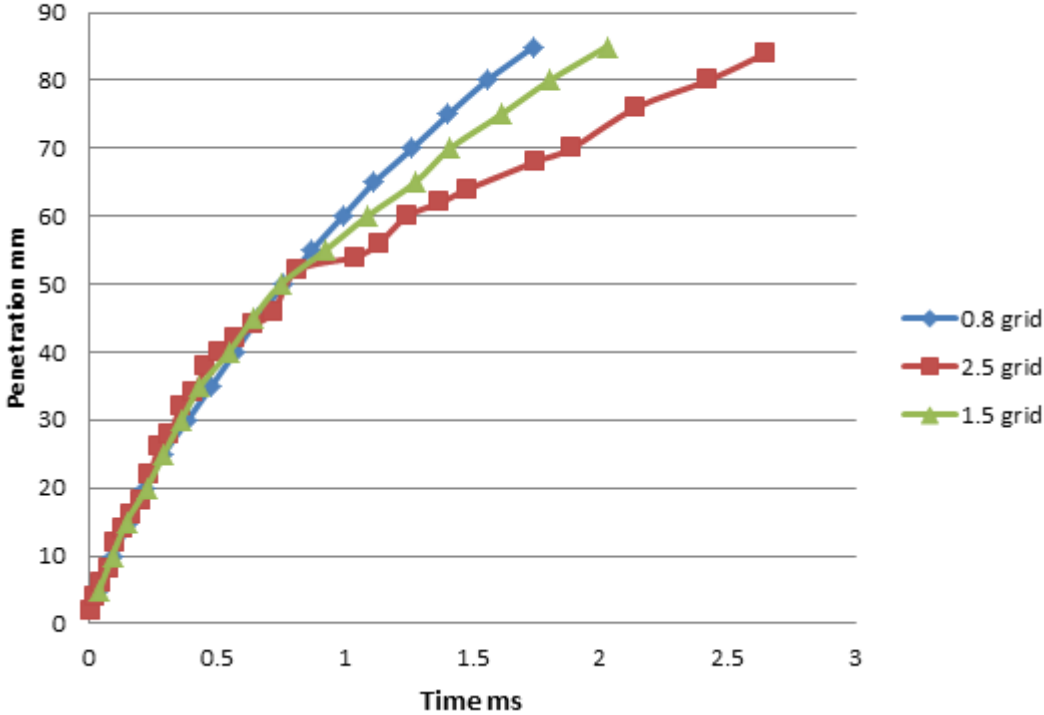


Figure 4.9: Grid sensitivity test for ILASS

of fluid particle. In addition to that the sprays with different breakup models are also compared which gives lot of variation .

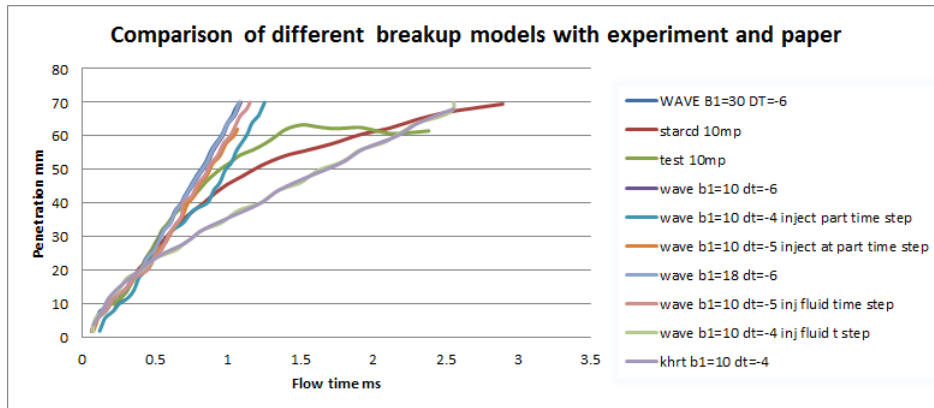


Figure 4.10: Comparison of Spray penetration with different breakup Models for of ICLASS

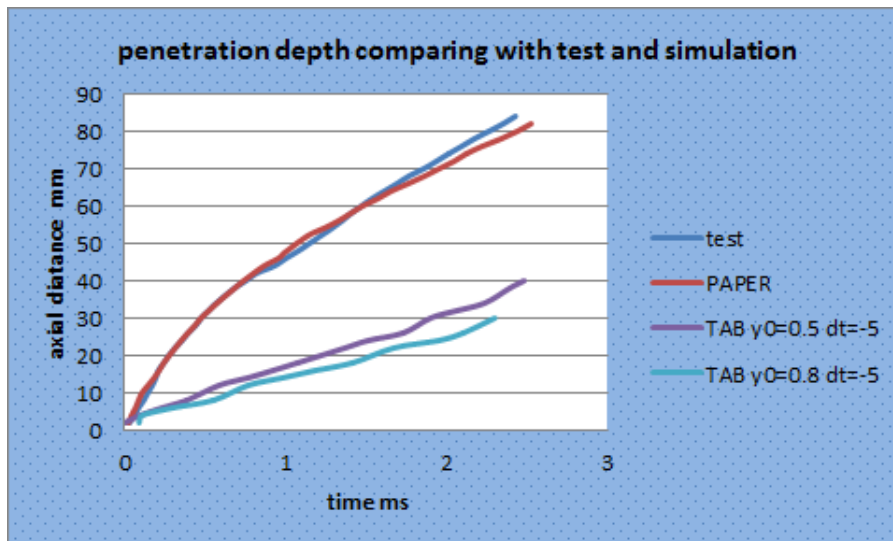


Figure 4.11: Comparison of Spray penetration with different breakup Models for ILASS

For ILASS paper the best result which we find after so many simulations run with change in timestep and the time constant B1 for a wave beakup model is at e-05 as particle flow timestep and breakup time constant B1=20(shown in Fig 4.19)

### close to result wave breakup model(ICLASS)

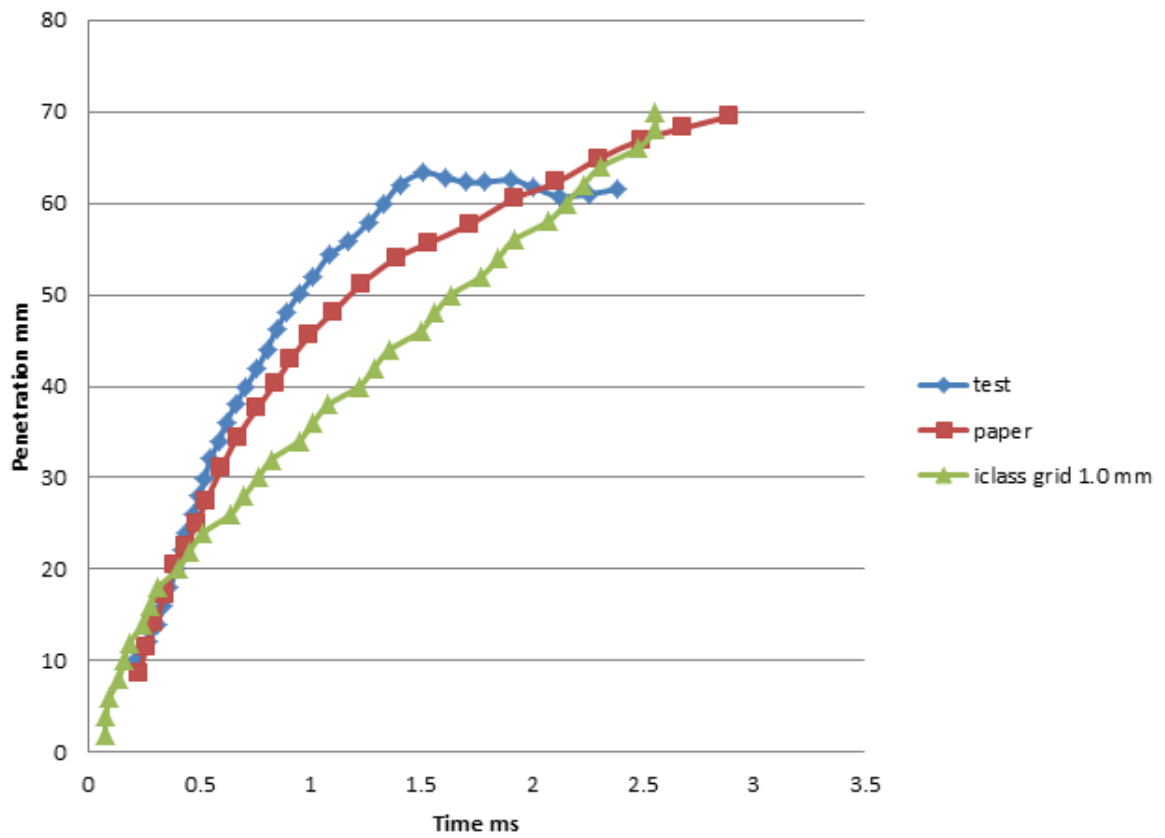


Figure 4.12: Spray penetration curves matching with test results ICLASS

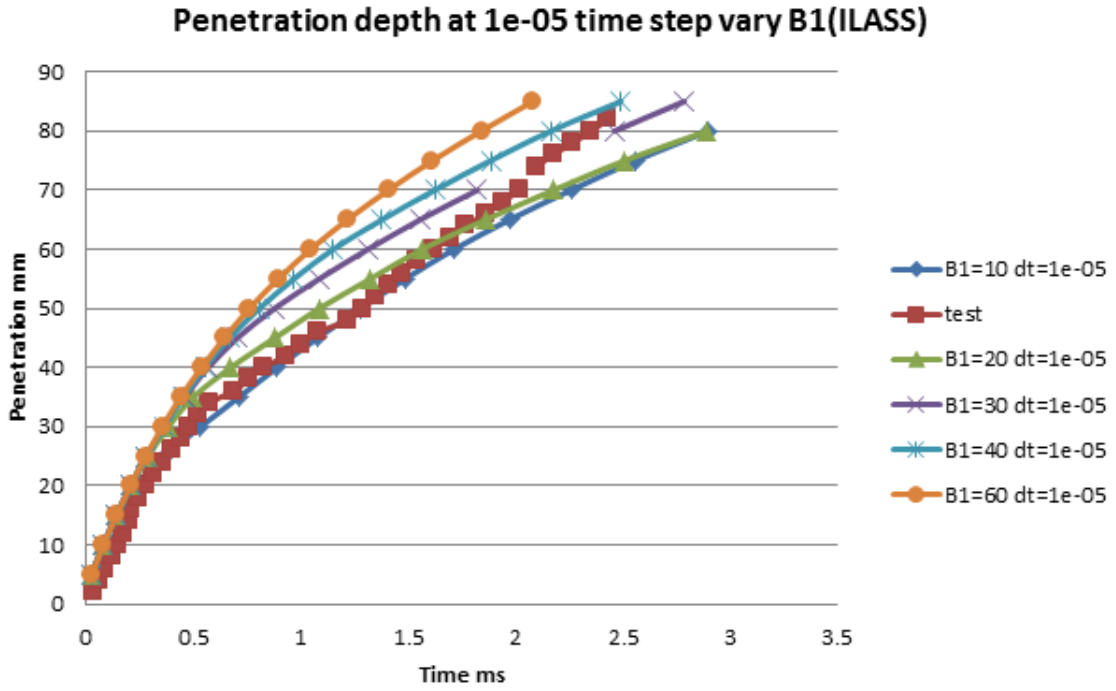


Figure 4.13: Spray penetration depth at 1e-05 time step by varying B1(ILASS)

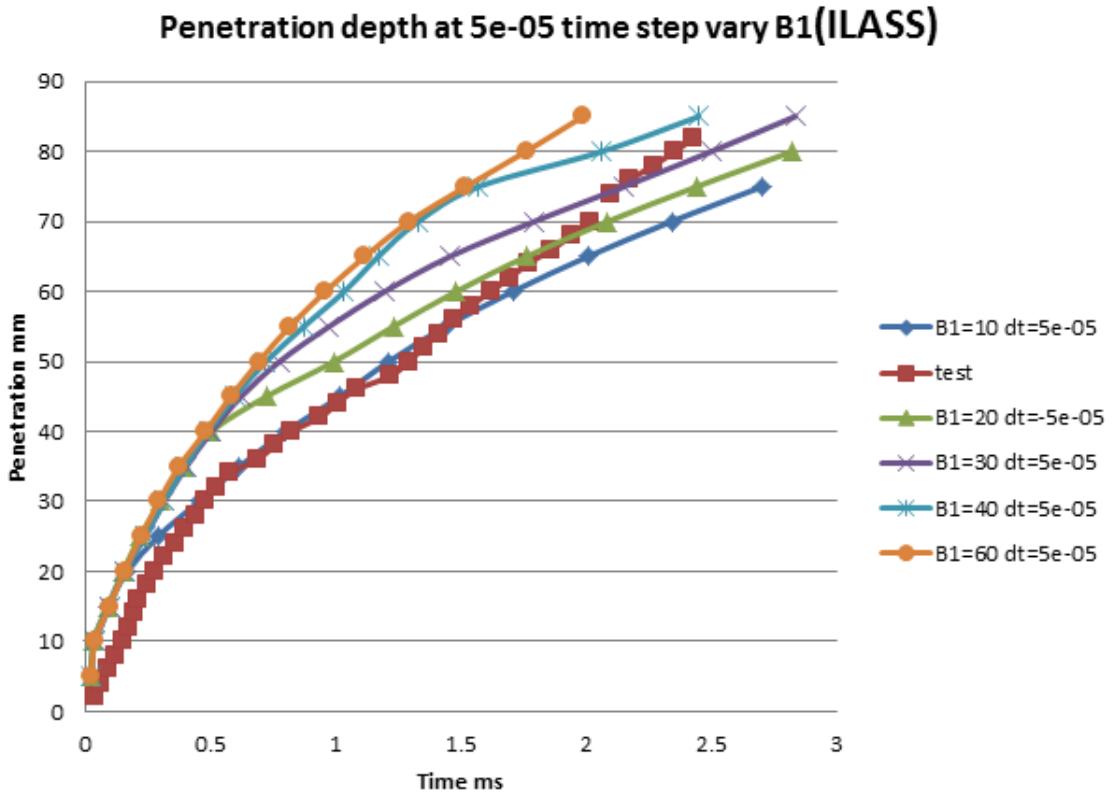


Figure 4.14: Spray penetration depth at 5e-05 time step by varying B1(ILASS)

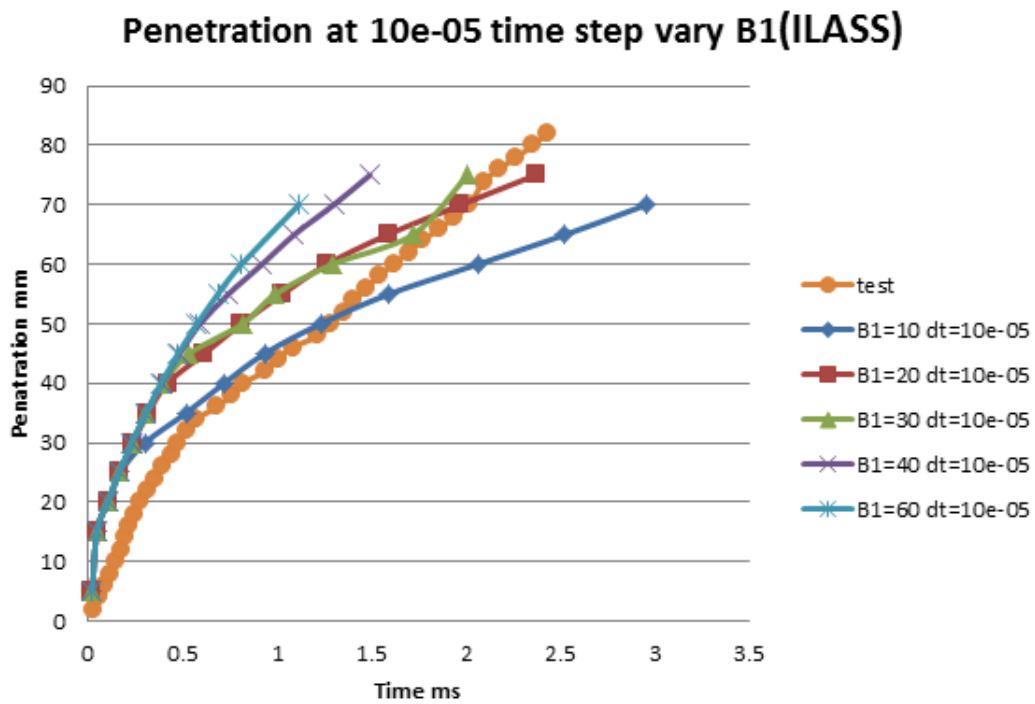


Figure 4.15: Spray penetration at 10e-05 time step by varying B1(ILASS)

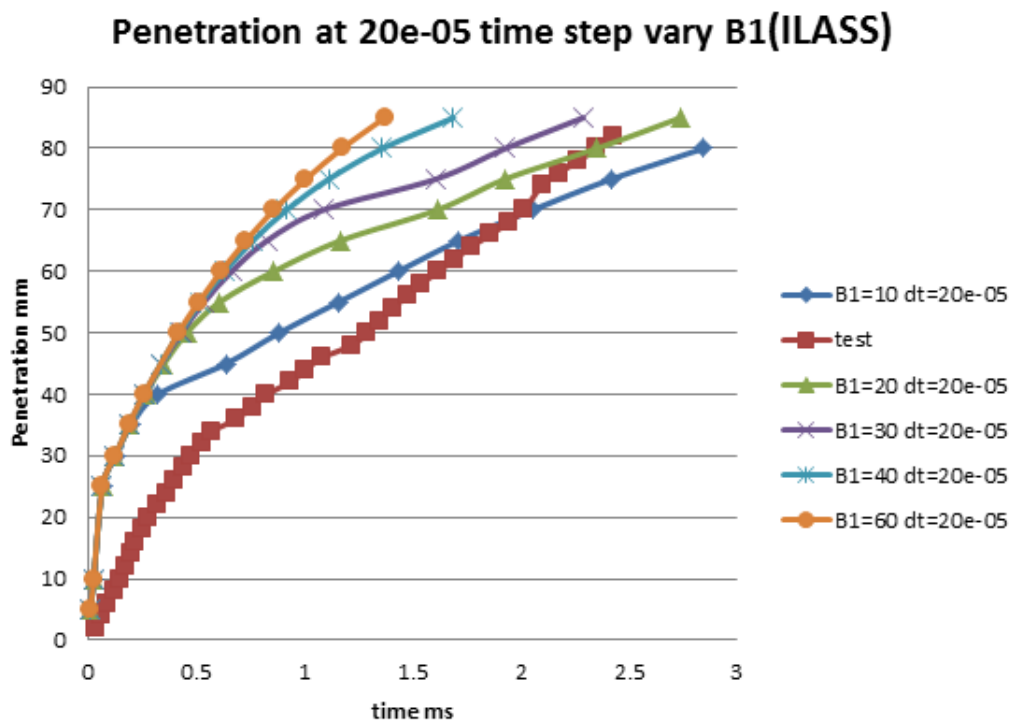


Figure 4.16: Spray penetration at 20e-05 time step by varying B1(ILASS)

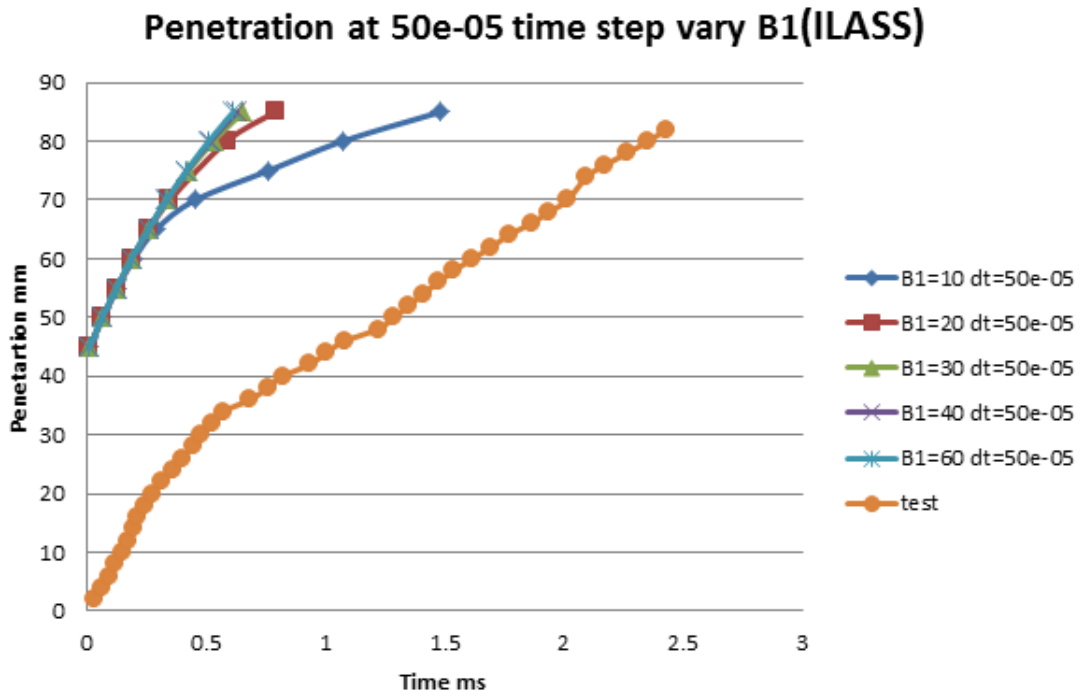


Figure 4.17: Spray penetration at 50e-05 time step by varying B1(ILASS)

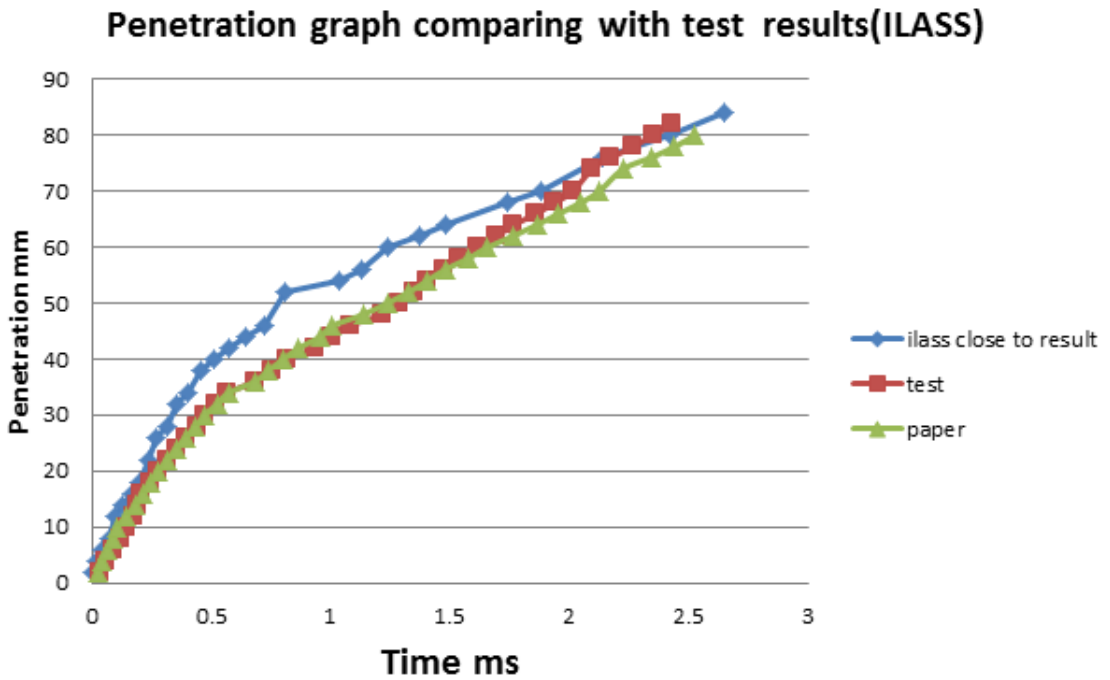


Figure 4.18: Spray penetration curves comparing with test results(ILASS)

**Physical Properties** Fluent's DPM model is extensively used to model evaporating,(We used droplet dodecane and octane sprays). This is done with special attention for temperature dependent material properties and for many different setups, including various meshes, solver timesteps and amount of parcels. The results are compared with a measurement on the Laser Sheet Imaging and Phase Doppler Particle Analyzer experimental data from the literature of ILASS . From these comparisons it is found that the DPM model gives unsatisfactory results concerning spray and liquid lengths. Nevertheless, some best practice setups resulted from this study, which are at least valid for octane sprays in engine like conditions. That are  $2.5 \text{ mm}^3$  cells aligned with the spray axis and solved with a solver time step of e-6 s, and injection of 5 parcels per timestep. Besides these numerical features, setting material properties as function of temperature is probably the most important. Spray formation includes thermodynamic interaction between two phases with large temperature differences in a high pressure environment. Therefore material properties play an important role in spray modeling, even in the case of inert sprays. The material properties in Fluent are set as function of temperature with data from the thermo-physical database of DIPPR[26]. Especially the specific heat, vapor pressure and boiling point are key properties that have a big influence on the results. In approximately the first 0.5 ms the model estimates too large lengths. This is due to the assumed constant mass flow in the numerical case, whereas in (Laser Sheet Imaging and Phase Doppler Particle Analyzer tests) practice the mass flow takes some time to develop after the injection starts . To account for this phenomenon the mass flow is to be increased gradually. But for the sake of simplicity this is kept constant because in Fluent changing mass flow is a manual process unfortunately there is no other easier way to do so in Fluent.

One can see that the start of the injection is predicted much better, but thereafter, as expected, the penetration lags behind the measured curve. From many simulations of the ILASS paper nad ICLASS paper similar trends as for the Laser Sheet Imaging and Phase Doppler Particle Analyzer tests are found, therefore only the best practice result is shown in Figure 4.10. From the former considerations best practice means the  $2.5 \text{ mm}^3$  square mesh with a solver time step of e-6 seconds, and of course also this time temperature dependent material properties are used. Now, the Mass flow is kept constant for further parametric study on time ,temperature of fuel /air and pressure for the time being and studied how spray penetration curves deviate from the base case.

The operating conditions plays an important role in the spray penetration measurement because if the temperature of surrounding air increases the air become lighter and the particle can easily penetrate through it.So penetration increases .But at the same time the evaporation also increases which the particle vanishes on its way.

Out of this two which one is dominating can be found from the parametric study on change in temperature , pressure and ultimately density.

### **Parametric study on change in Ambient temperature ,pressure and fuel injected temperature**

So from the figure 4.19 ,it was clear for the change in ambient temperature (rise) there are variation in penetration profile.

As the temperature increases from 300K ,500K to 700K the penetration increases .This tells the temperature plays an important role and some interrelation between the temperature with penetration should be found.

Similarly change in pressure (shown in fig 4.20)from 1.1MPa, 3MPa and 5MPa the penetration of spray curves are found.It was very much clear that penetration rapidly decreases with increase in pressure of surrounding gas(increase in denseness of surrounding gas)

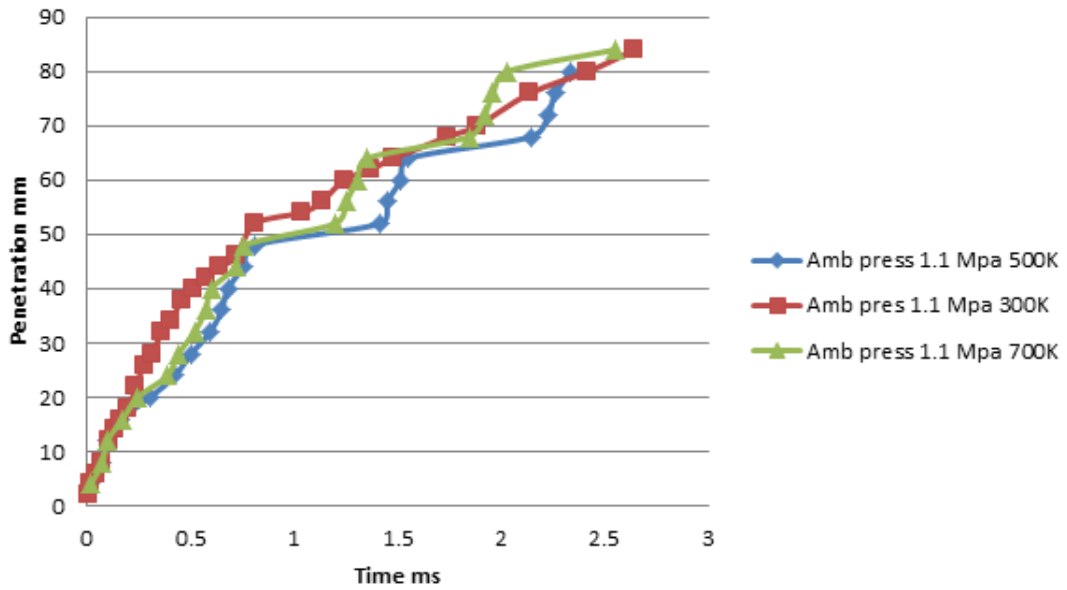
In the same way the change in fuel temperature(shown in fig 4.21) of the fuel spray from 290 K,300 K,310 K,320 K the variations are not much initially .But after some time (1.5ms) there was substantial variation which tells spray penetration decrease with fuel temperature increase and as time passes again there was substantial increment shows for 320K.

Overall one can conclude that also for the Laser Sheet Imaging and Phase Doppler Particle Analyzer tests spray the results are not satisfactory.

### **Paramteric study on physical properties of gas and fuel**



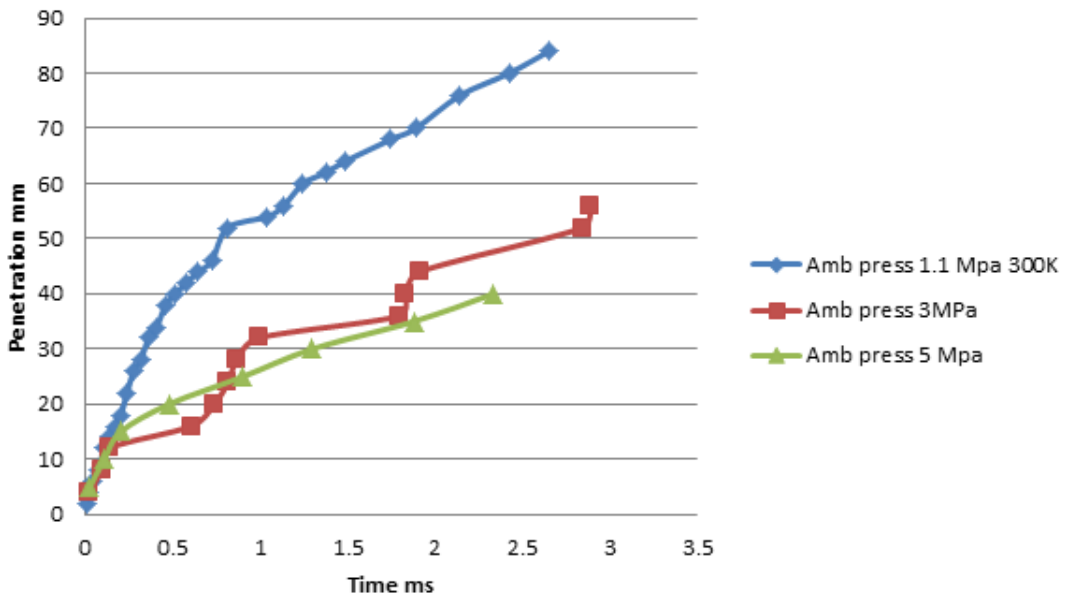
### Parametric Study Vary Temp



[h]

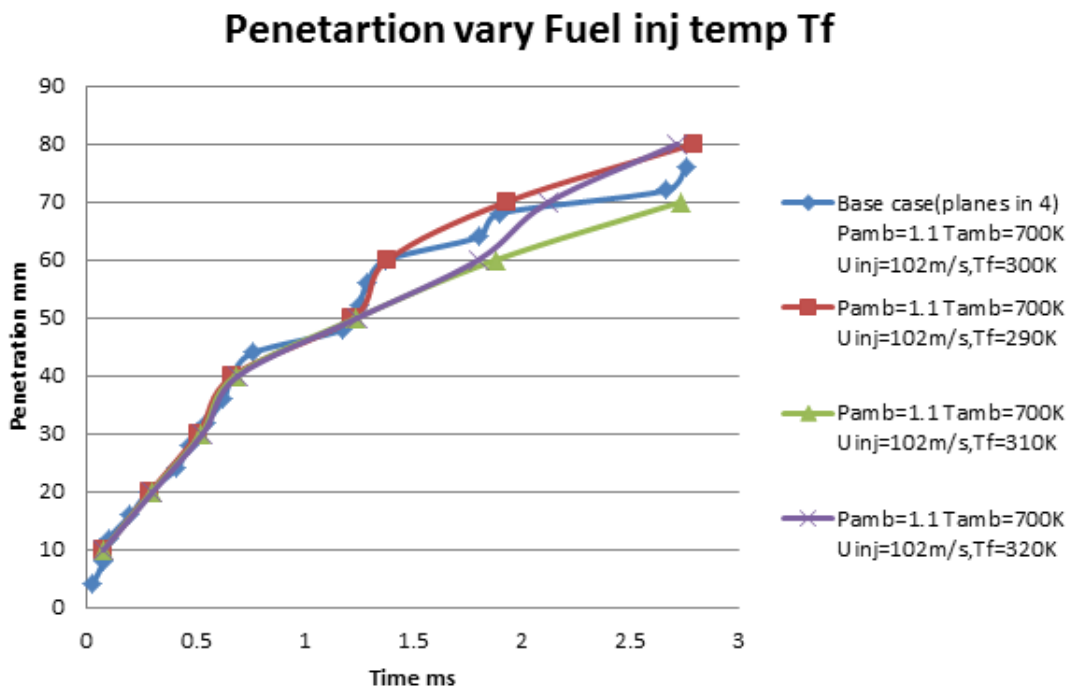
Figure 4.19: Spray penetration curves by varying ambient temperature

### Parametric study change in pressure



[h]

Figure 4.20: Spray penetration curves by varying ambient pressure



[h]

Figure 4.21: Spray penetration curves by varying fuel injected temperature

## 4.4 Dynamic or Deforming Mesh

There are three methods used for deforming mesh: spring-based smoothing, remeshing and layering [Fluent Manual].

In the spring-based method, the entity of the mesh volumes could be compared to a sponge. The nodes of the mesh will move in case of a movement of a boundary. So the mesh volumes get bigger or smaller, according to the movement of the piston. The remeshing method marks the faces that have to be remeshed according to the minimum and maximum length scales and the maximum cell skewness. Those faces are usually close to the moving boundaries. The third method, layering, is used to add or remove layers of neighboring cells to a moving boundary. This is a motion suitable for linear movement [Fluent] and so, this is used to simulate the movement of the piston. Layers are being added, when the piston goes down, subsequently they will be removed during the compression stroke. Figure 4.22 shows the mesh of the model of the cylinder at crank angle  $0^{\circ}$ ,  $90^{\circ}$  and  $180^{\circ}$ . To be able to run calculations on this model, it has to be meshed first. This was executed in

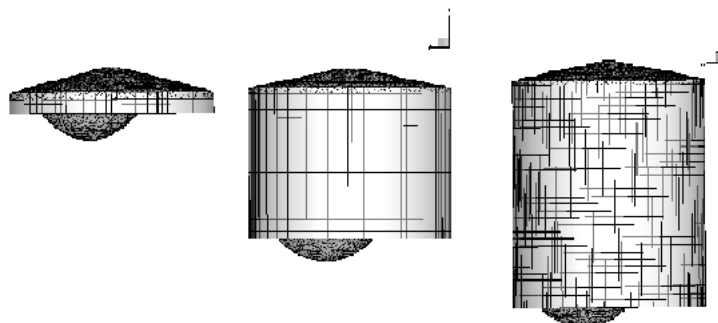


Figure 4.22: Dynamic Meshing Methods applied to Incylinder GDI engine

16397 cells	51893 cells	79037 cells
-------------	-------------	-------------

ICEMCFD, and since in this case there are moving parts involved (piston) the dynamic mesh option was employed. To simulate the piston moving down and upwards, its mesh creates new volumes, using the layering option in the dynamic mesh menu. The boundary conditions have to be put in ICEMCFD. This is needed to define where the fluid can pass and where it can't. Faces not defined will automatically be considered as walls. The piston has to be defined in order to be set to move. To initiate the simulation in Fluent, the mesh has to be imported and the dynamic mesh has to be set.

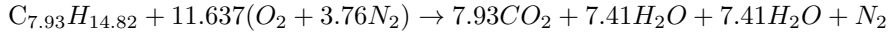
The Incylinder model of dynamic mesh (fluent) has the following inputs which are shown in Table 4.6.

Table 4.6: Table showing the inputs for Incylinder option in Dynamic mesh of Fluent

Crank shaft Speed	1200	rpm
Starting Crank Angle	180	Degrees
Crank Period	720	Degrees
Crank Angle Step Size	0.5	Degrees
Piston Stroke	76	mm
Connecting rod Length	145	mm
Piston Stroke Cutoff	0	mm
Minimum Valve Lift	0	mm

**Illustration of the Mixing Strategy** In an actual DIG engine, the strength of the reverse tumble vortex would depend on the intake port and valve design, number and placement of valves, valve actuation and control strategy, and engine operating conditions. In order to decouple our investigation from the details of the intake system design, as well as to expedite the numerical simulation, runs were conducted for the closed part of the cycle only. While the equivalence ratio prescribed in this manner would be somewhat different than the port-generated one in an actual engine, this approach offers attractive flexibility and is still very useful for conceptual studies. In this study, the fuel is injected late in compression and directed toward the spherical piston cavity. Subsequently, the spray is redirected towards the spark plug by the reverse tumble and the impingement action on the cavity surface. The spacing between the fuel injector and the spark plug is intentionally wide to provide additional time for fuel breakup, evaporation and mixing with air. Thereby, an air-fuel mixture of desired mixture strength can be prepared around the spark plug by the moment of spark firing. While Kume et al.[27] have demonstrated this injection strategy for equivalence ratios up to 0.5 (low loads), we will explore whether it is possible to use this strategy with full load operation (=1.0/0.8/1.2). The fluid mechanics associated with late fuel injection are illustrated for a baseline case in Table 4.6, and further calculation for equivalence ratio in terms of mass fraction was derived below which tracks flow and mixing histories at different instants during compression.

**Incylinder Model Calculations for Base Case( =0.8)**



$$\left(\frac{F}{A}\right)_{stoi} = \left[\frac{11.637(3.76 \times 28)}{114}\right] = \frac{1}{14.52} = 0.06889$$

$$\phi = \left[\frac{\frac{F}{A}_{act}}{\left(\frac{F}{A}\right)_{stoi}}\right]$$

$$\left(\frac{F}{A}\right)_{act} = \frac{1}{14.52} \times 0.8 = 0.055$$

$$\dot{m}_{fcycle} = 0.055 \times \dot{m}_{acycle}$$

$$\dot{m}_{acycle} = \rho_g \times V_{total}$$

$$\dot{m}_{fcycle\Delta\theta} = \frac{0.055 \times \dot{m}_a}{T \times 8} 1200rpm = 20rps$$

$$2rotations = 1cycle$$

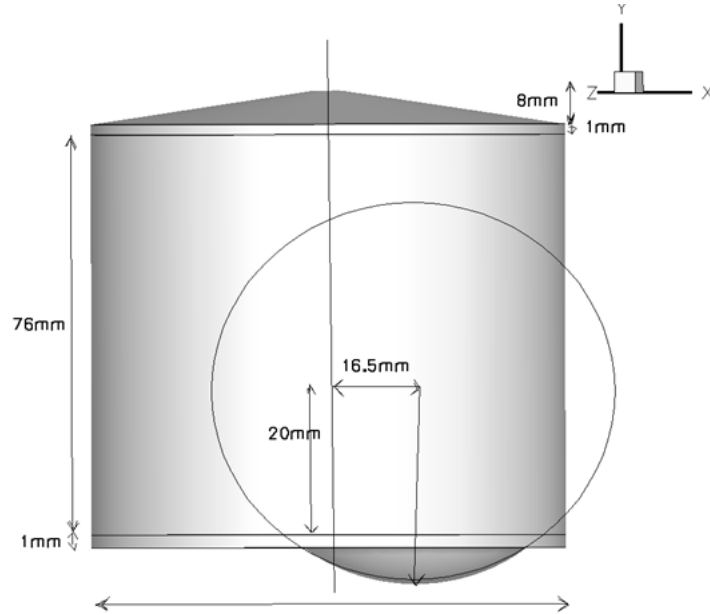


Figure 4.23: Schematic diagram of cylinder geometry with piston bowl showing various dimensions

10cycles  $\rightarrow$  1second

1cycle  $\rightarrow$  110<sup>th</sup>second

720<sup>o</sup>  $\rightarrow$   $\frac{1}{10}$ <sup>th</sup>second

20<sup>o</sup>  $\rightarrow$   $\frac{1}{10} \times \frac{7}{720}$ seconds

### Derivation to find the equivalence ratio in terms of mass fraction

Let

$$\text{mass fraction} = \frac{m_v}{m_v + m_a} = M_F$$

$$\frac{1}{M_F} = \frac{m_v + m_a}{m_v} = 1 + \frac{m_a}{m_v}$$

$$\frac{m_a}{m_v} = \frac{1}{M_F} - 1$$

$$\frac{m_v}{m_a} = \frac{m_f}{m_a} = \left[ \frac{1}{M_F} - 1 \right]^{-1}$$

We know

$$\left( \frac{m_f}{m_a} \right)_{stoi} = \frac{1}{14.52} = \left[ \frac{1}{M_F} - 1 \right]^{-1}$$

$$\frac{1}{(M_F)_{stoi}} - 1 = 14.52$$

$$\left( \frac{1}{M_F} \right)_{stoi} = 15.52$$

$$(M_F)_{stoi} = (15.52)^{-1} = 0.06889$$

Therefore, from definition equivalence ratio( the actual Mass fraction we directly get from Fluent)

Table 4.7: Engine Specifications useful for our present study

Engine Specification	Number	Unit
GDI engine	4 Stroke	2 Rotations=1 cycle
Speed Ranges	1200-1800	Rpm
Compression ratio	9.79	No unit
<i>Bore × stroke</i>	$85 \times 77$	mm

Table 4.8: Baseline for the parametric study on moving piston

Stationary Volume Zone	0.000024387	$m^3$	Measured
Deforming Volume Zone	0.000436690	$m^3$	Measured
Rigid Volume Zone	0.000018709	$m^3$	Measured
Total Volume	0.000479786	$m^3$	Measured
Closed Loop temperature and pressure when piston is at BDC	427 0 <sup>C</sup> 700K	101325 Pa	
Density of air charge	0.504	$Kg/m^3$	
Density of Fuel Charge at 343 K	663	$Kg/m^3$	
Molecular Wt	114.22	Kg/Kgmol	
Mass of air in cylinder	0.00025951	Kg/cycle	=Density of air *Total Volume

$$\phi = \frac{[M_F]_{actual}}{[M_F]_{Stoi}} = \frac{[\frac{1}{M_F} - 1]}{0.06889}$$

By creating a custom field function in the fluent from the known terms we get the equivalence ratio and in this way we can plot the contours also. From this contours we can able to identify the stratification of the fuel-air mixture.

The Tables below give us the idea behind the stratification of GDI engines by injecting sprays at different CA timings (i.e., in turn varying flow and velocity of injection ).From Wall film height contours at cylinder head, wall and on piston given the idea how the piston bowl had its effect and film formation decreases. In addition to that the Tumble ratio (a dimensionless number which signifies Tumble effect in terms of engine speed) at different CA from start to end of TDC was also monitored .From this curves the Tumble ratio range can be found for minimum wall films and a good stratification possible at sparkplug.

Table 4.9: Table giving the details of flow, velocity, time period for parametric study at equivalence ratio=0.8

Speed (rpm)	Time period of Injection (CA)	Time (seconds)T	Mass flow rate of fuel/Orifice (kg/s)	Velocity of fuel injection (m/s)
1200	20	2.777xe-3	6.47xe-4	13.80
	40	5.555xe-3	3.23xe-4	6.92
1500	20	2.222xe-3	8.02xe-4	17.70
	40	4.444xe-3	4.04xe-4	8.66
1800	20	1.851xe-3	9.70xe-4	20.70
	40	3.703xe-3	4.85xe-4	10.39

Table 4.10: Table giving the details of flow, velocity, time period for parametric study at equivalence ratio=1.0

Speed (rpm)	Time period of Injection (CA)	Time (seconds)T	Mass flow rate of fuel/Orifice (kg/s)	Velocity of fuel injection (m/s)
1200	20	2.777xe-3	7.761xe-4	16.61
	40	5.555xe-3	3.879xe-4	8.302
1500	20	2.222xe-3	9.699xe-4	20.75
	40	4.444xe-3	4.849xe-4	10.37
1800	20	1.851xe-3	11.64xe-4	24.91
	40	3.703xe-3	5.820xe-4	12.45

Table 4.11: Table giving the details of flow, velocity, time period for parametric study at equivalence ratio=1.2

Speed (rpm)	Time period of Injection (CA)	Time (seconds)T	Mass flow rate of fuel/Orifice (kg/s)	Velocity of fuel injection (m/s)
1200	20	2.777xe-3	9.305xe-4	14.94
	40	5.555xe-3	4.655xe-4	9.96
1500	20	2.222xe-3	11.63xe-4	24.89
	40	4.444xe-3	5.819xe-4	12.45
1800	20	1.851xe-3	13.97xe-4	29.90
	40	3.703xe-3	6.984xe-4	14.94

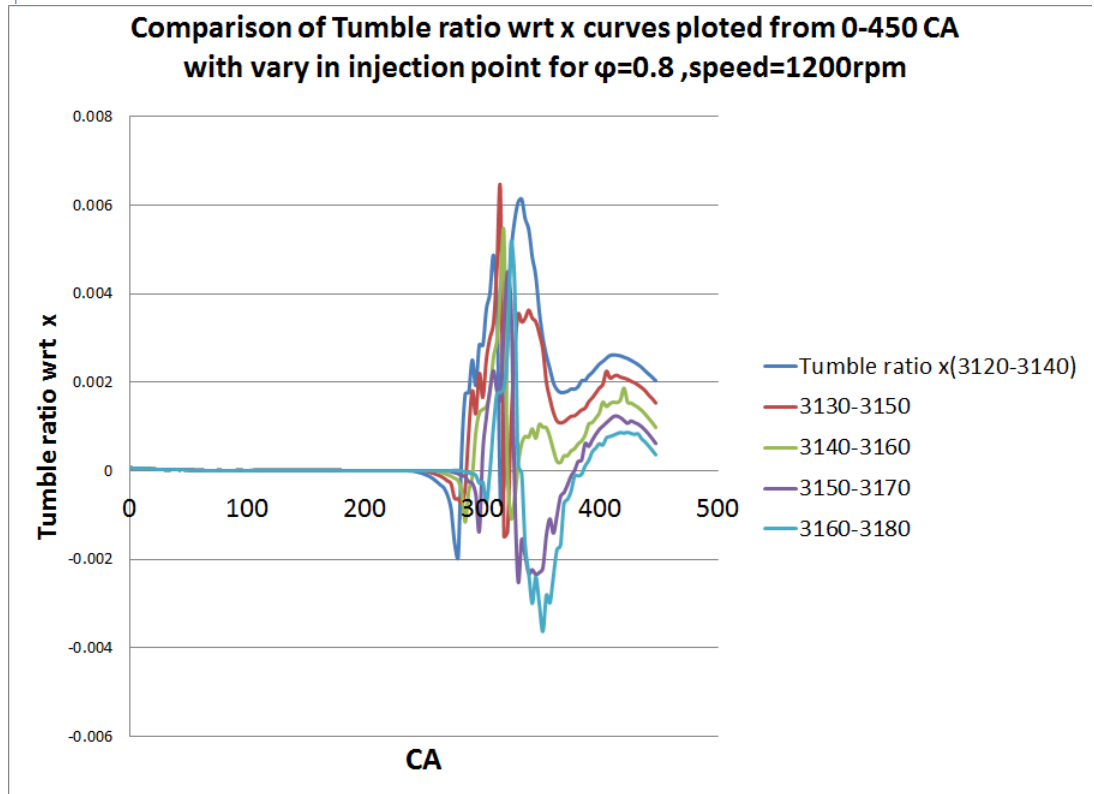
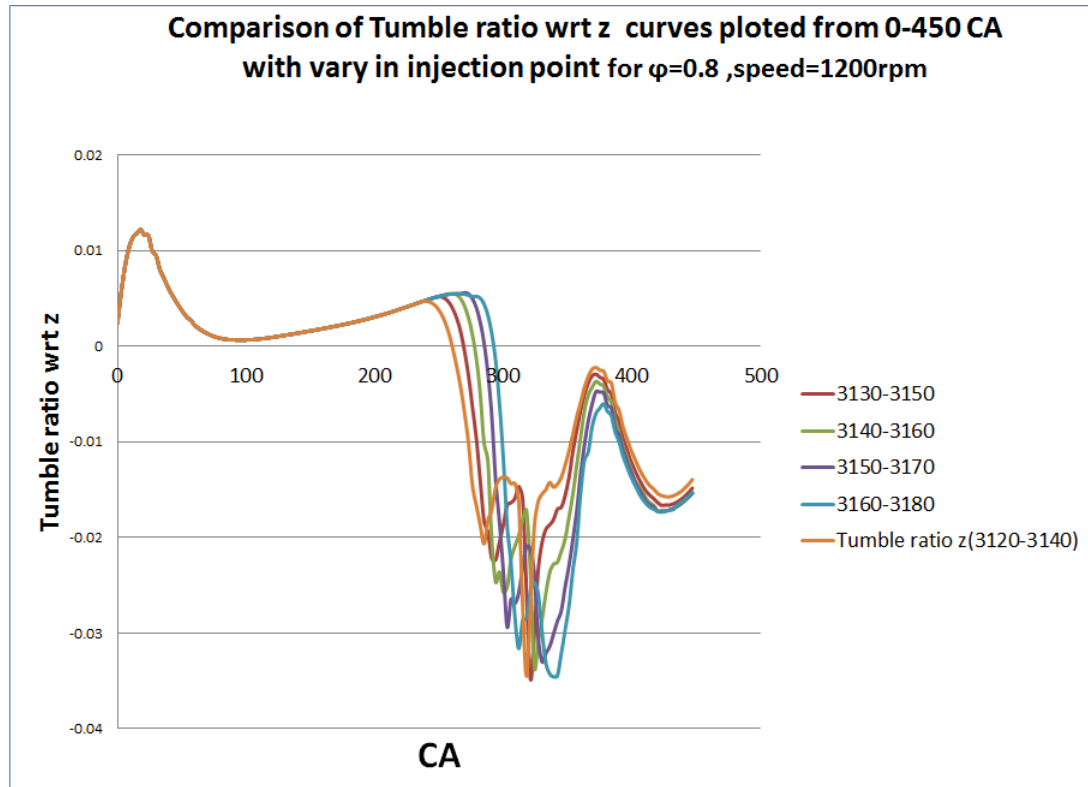


Figure 4.24: Tumble Ratio curves inside cylinder wrt Z and X axis(perpendicular to cylinder axis) at  $\Phi = 0.8$  ,speed=1200rpm by varying injection point



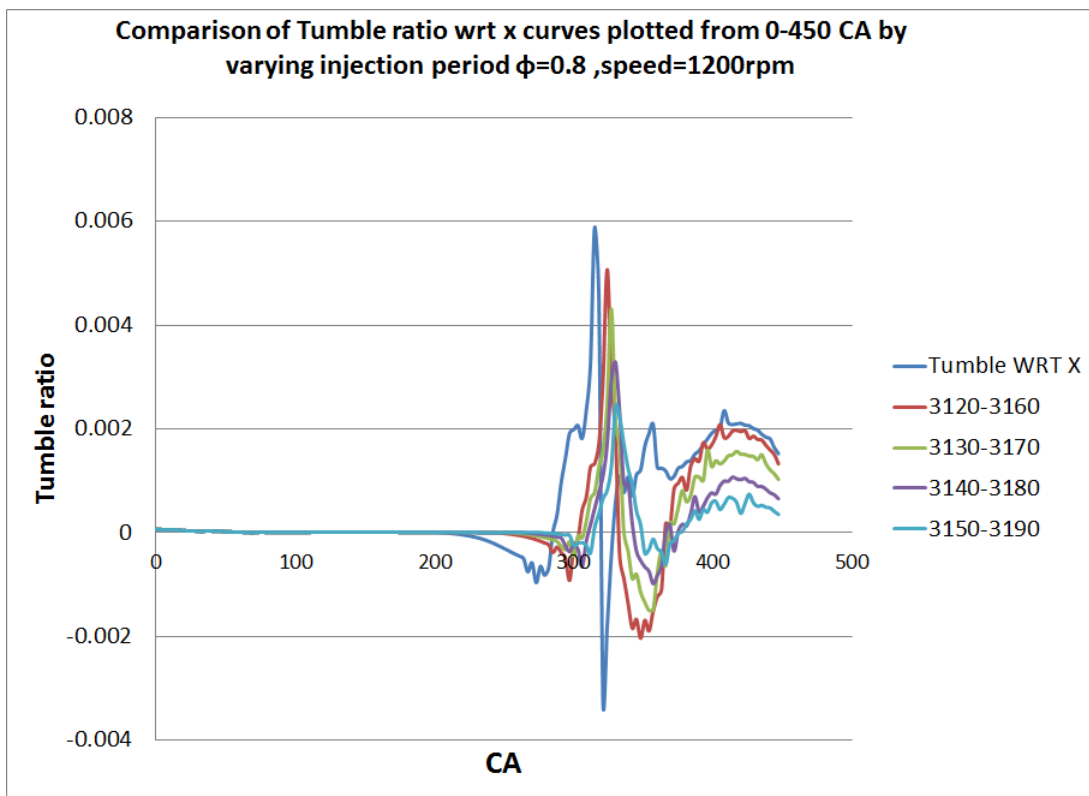
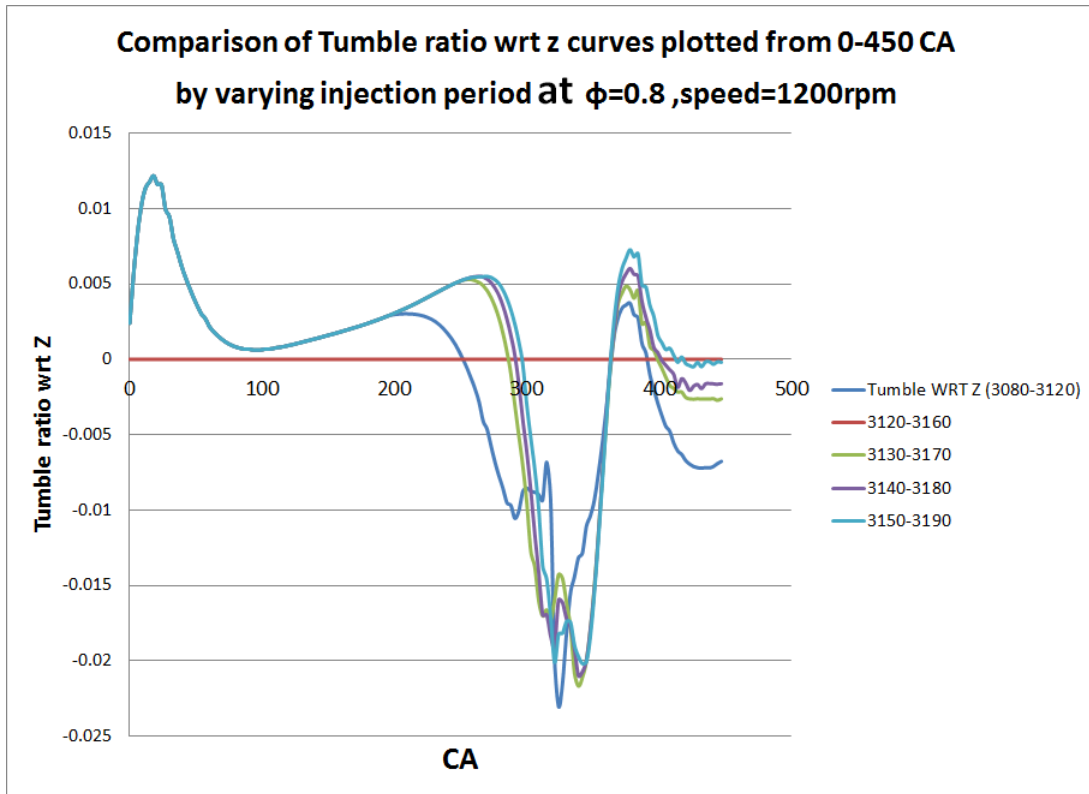


Figure 4.25: Tumble Ratio curves inside cylinder wrt Z and X axis(perpendicular to cylinder axis)at  $\Phi = 0.8$ , speed=1200rpm by varying injection period

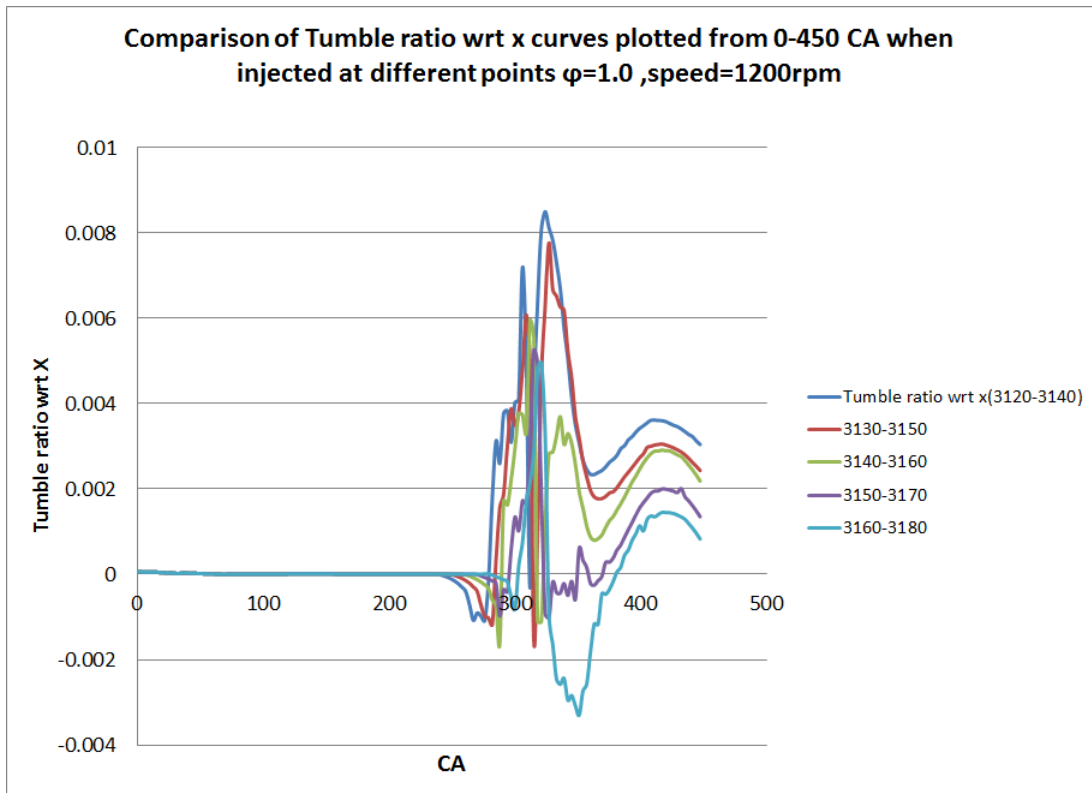
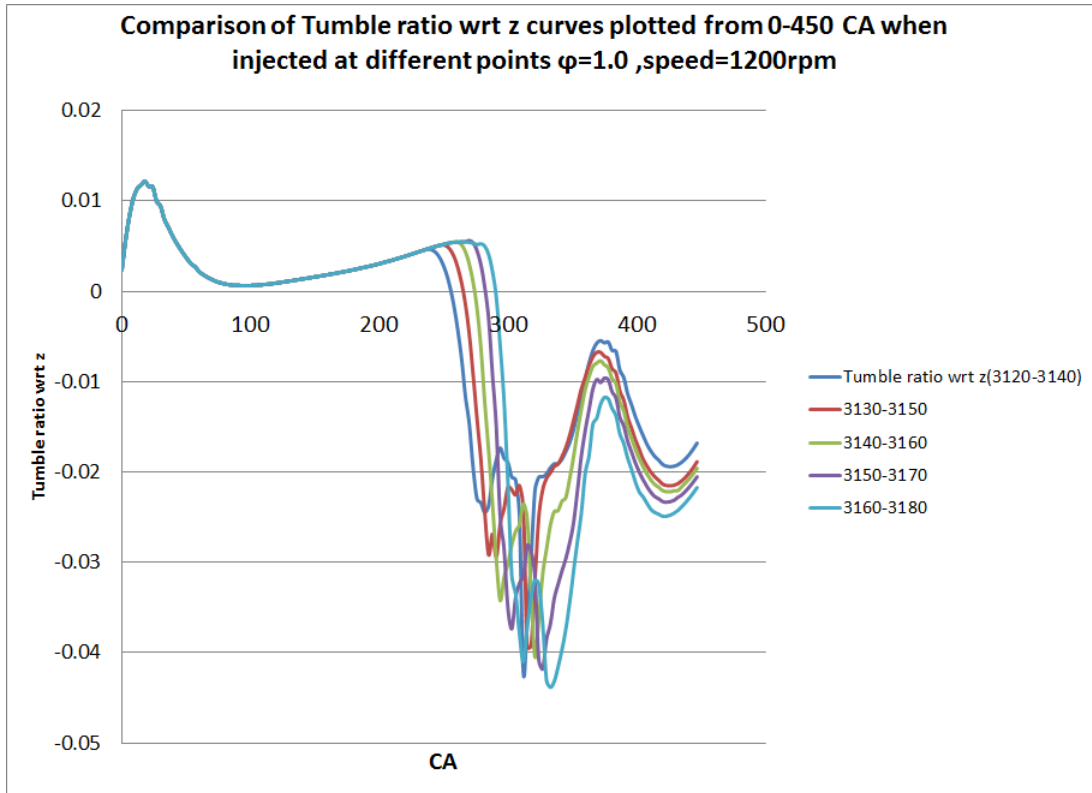


Figure 4.26: Tumble Ratio curves inside cylinder wrt Z and X axis(perpendicular to cylinder axis)at  $\Phi = 1.0$ , speed=1200rpm

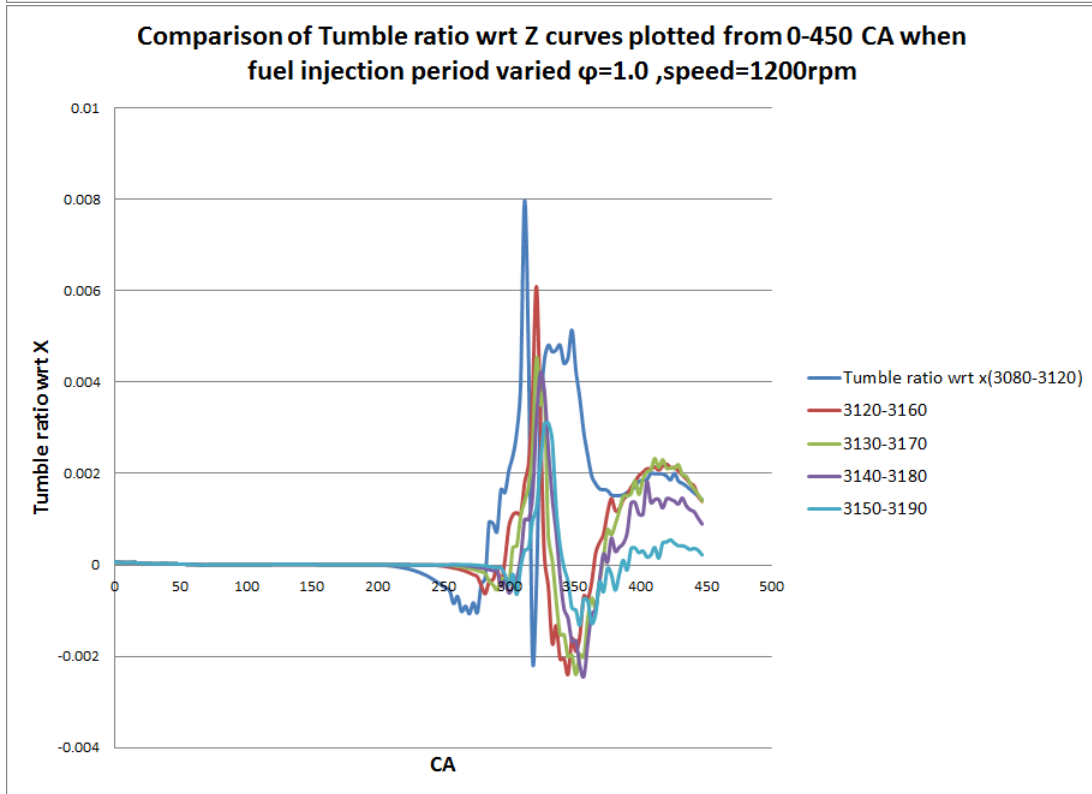
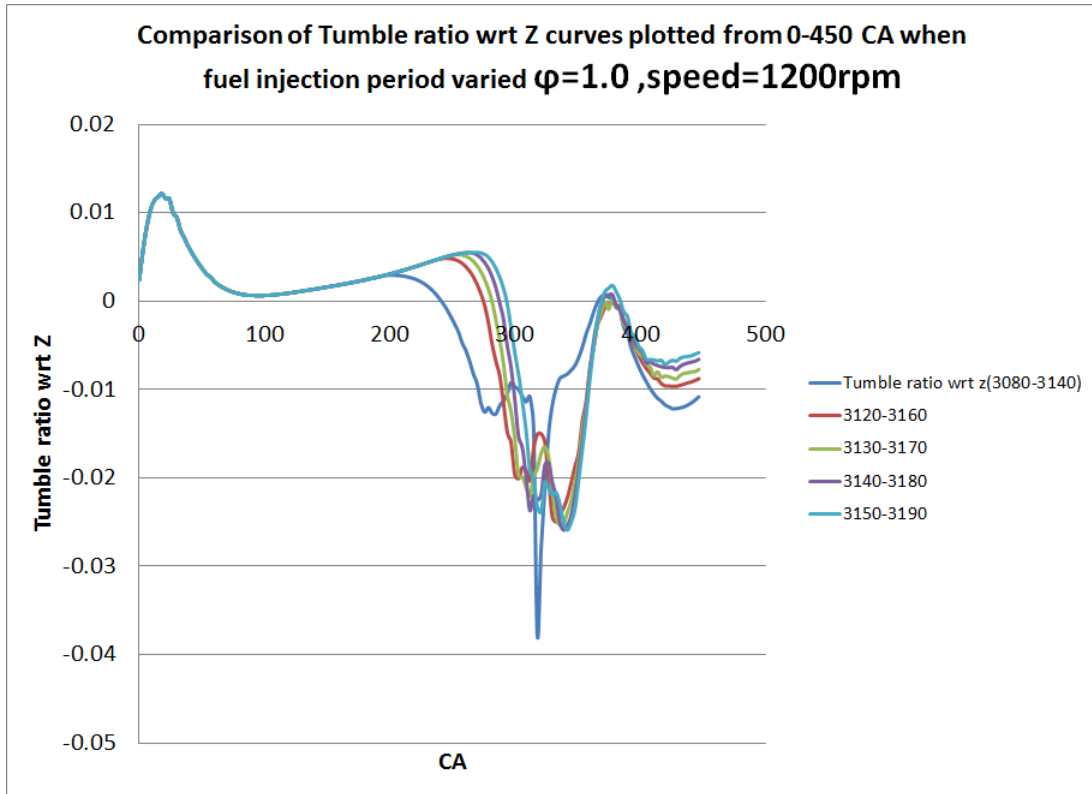


Figure 4.27: Tumble Ratio curves inside cylinder wrt Z and X axis(perpendicular to cylinder axis)at  $\Phi = 1.0$  ,speed=1200rpm

Table 4.12: Table describes the operating conditions with spray penetration snapshots at different particle Flow time

Temp at BDC	Bore to stroke( $D \times L$ )	Injector Location	(42,77,0)
$700^0K$	(85mm $\times$ 77mm)		
$P_{air}$	Solid cone eight injectors Time from SOI $\Delta\theta$		
0.1MPa			

Table 4.13: Parametric study on the equivalence ratio for finding effective stratification for different injection point

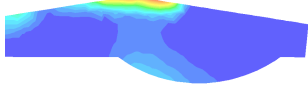
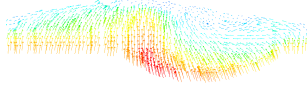
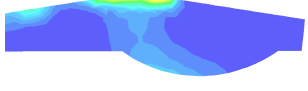
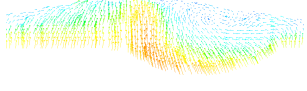
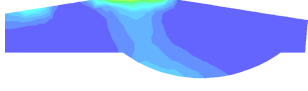
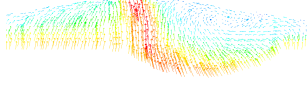
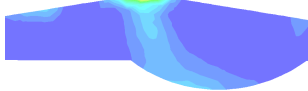
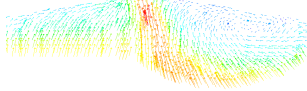

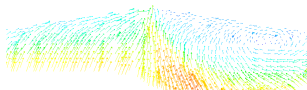
$\phi = 0.8, \Delta\theta = 20^\circ$  240-260	Equivalence ratio contours at the CA where spark occurs  	Velocity vectors showing the tumble effect  
250-270		
260-280		
270-290		
280-300		

Table 4.14: Parametric study on the equivalence ratio for finding effective stratification for different injection period

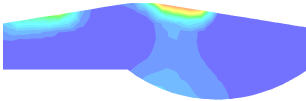
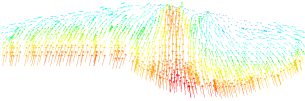

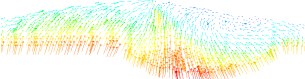

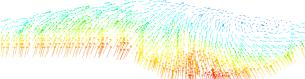

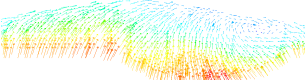

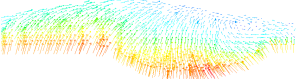
$\phi = 0.8, \Delta\theta = 40^\circ$  200-240	Equivalence ratio contours at the CA where spark occurs  	Velocity vectors showing the tumble effect  
240-280		
250-290		
260-300		
270-310		

Table 4.15: Parametric study on the equivalence ratio for finding effective stratification for different injection point

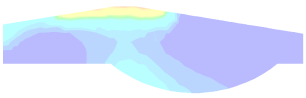
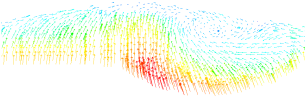
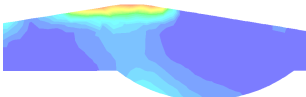
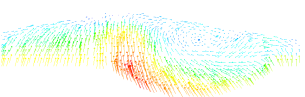
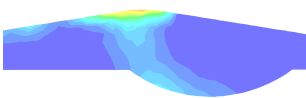
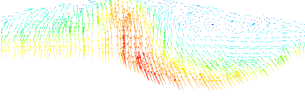
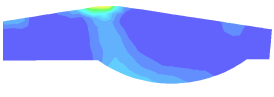
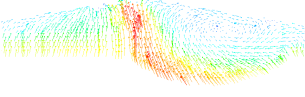
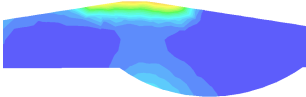
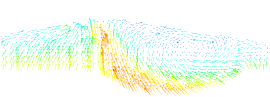
$\phi = 1.0, \Delta\theta = 20^\circ$  240-260	Equivalence ratio contours at the CA where spark occurs  	Velocity vectors showing the tumble effect  
250-270		
260-280		
270-290		
280-300		

Table 4.16: Parametric study on the equivalence ratio for finding effective stratification for different injection period

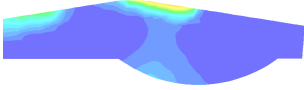
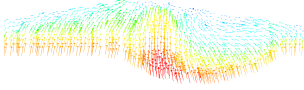
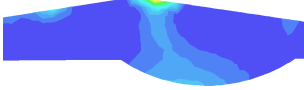
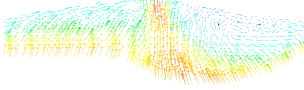

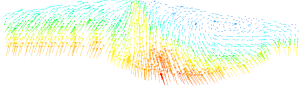

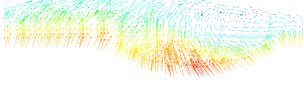

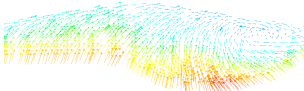
$\phi = 1.0, \Delta\theta = 40^\circ$  200-240	Equivalence ratio contours at the CA where spark occurs  	Velocity vectors showing the tumble effect  
240-280		
250-290		
260-300		
270-310		



Table 4.17: Parametric study on the equivalence ratio for finding effective stratification for different injection point

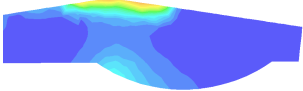
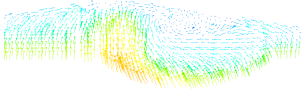
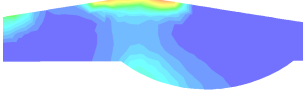
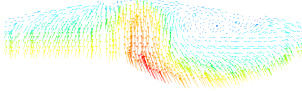
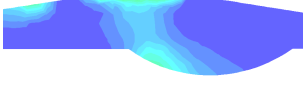
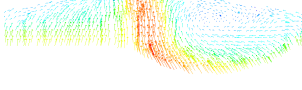
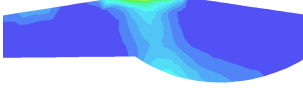
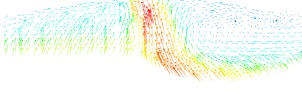

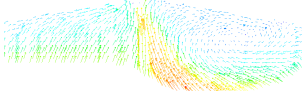
$\phi = 1.2, \Delta\theta = 20^\circ$  240-260	Equivalence ratio contours at the CA where spark occurs  	Velocity vectors showing the tumble effect  
250-270		
260-280		
270-290		
280-300		

Table 4.18: Parametric study on the equivalence ratio for finding effective stratification for different injection period

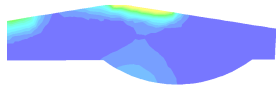
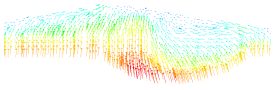
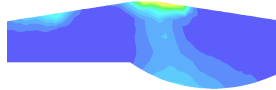
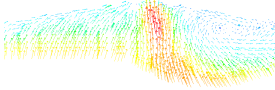
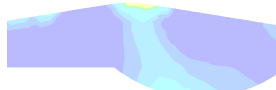
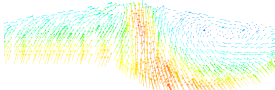
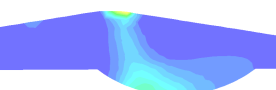
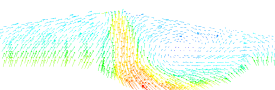

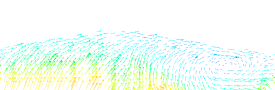
$\phi = 1.2, \Delta\theta = 40^\circ$  200-240	Equivalence ratio contours at the CA where spark occurs  	Velocity vectors showing the tumble effect  
240-280		
250-290		
260-300		
270-310		

Table 4.19: Parametric study on the equivalence ratio for finding effective stratification for different injection point

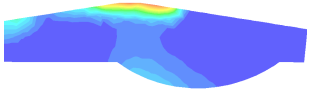

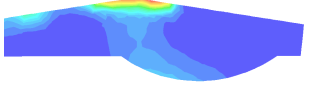
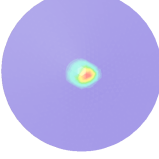
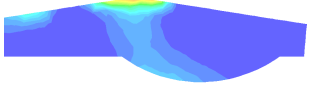
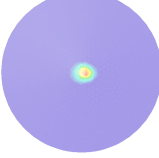
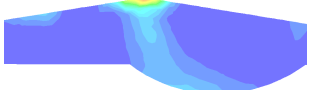
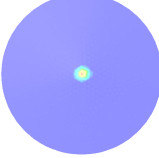

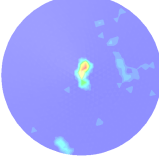
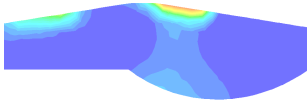
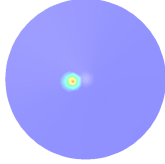

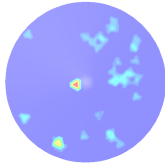

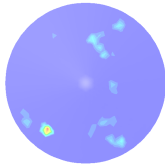

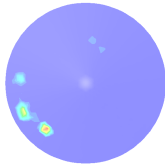

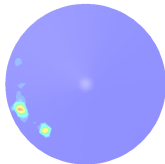
$\phi = 0.8, \Delta\theta = 20^\circ$  240-260	Equivalence ratio contours at the CA where spark occurs  	Wall film spread contours on head surface  
250-270		
260-280		
270-290		
280-300		

Table 4.20: Parametric study on the equivalence ratio for finding effective stratification for different injection period

$\phi = 0.8, \Delta\theta = 40^\circ$  200-240	Equivalence ratio contours at the CA where spark occurs  	Wall film spread contours on head surface  
240-280		
250-290		
260-300		
270-310		

# Chapter 5

## Conclusion

The work till now completed on spray Gasoline injections in the engine study is extensively used to model an evaporating sprays (We used inert dodecane and octane sprays for validation). This is done with special attention for temperature dependent material properties and for many different setups, including various meshes, solver timesteps and amount of parcels. The results are compared with a measurement on the Laser Sheet Imaging and Phase Doppler Particle Analyzer experimental data from the literature of ILASS . From these comparisons it is found that the DPM model of fluent gives unsatisfactory results concerning spray and liquid lengths. Nevertheless, some best practice setups resulted from this study, which are at least valid for octane sprays in engine like conditions. That are  $2.5mm^3$  cells aligned with the spray axis and solved with a solver time step of  $10^{-5}$  s for particle flow , and injection of 5 particle streams per timestep. Besides these numerical features, setting material properties as function of temperature is probably the most important.

From a numerical point of view there are also major disadvantages. One of them is the imposed limitation to mesh refinement which is far from desirable when detailed in-cylinder mixture formation and combustion are to be modeled. The second disadvantage is that the discrete phase part of the calculations cannot be parallelized, while those detailed investigations require fine resolution, thus expensive simulations.

From the stratification of fuel vapour point of view the work done had given an extra motivation for implementing things like inlet, outlet , piston bowl geometries and also with combustion model in the future .

# Bibliography

- [1] Mustafa Bahattin elik and Blent zdalyan *Gasoline direct injection*
- [2] I. Pielecha, K. Wislocki, J. Czajka and D. Maslennikov. *The Qualitative Spray Characteristics of High-Pressure Gasoline Injection System. ILASS Europe 2010, 23rd Annual Conference on Liquid Atomization and Spray Systems, Brno, Czech Republic, September 2010.*
- [3] Huihe Qiu and Chin Tsau Hsu , *Method of phase-Doppler anemometry free from the measurement-volume effect , 1999 Optical Society of America OCIS codes: 010.3920, 290.0290, 290.4020, 290.5850, 350.4990,*
- [3] Cemil Bekdemir, *Numerical Modeling of Diesel Spray Formation and Combustion, Master thesis.*
- [4] Stefano Fontanesi 1, Vincenzo Gagliardi 2, Simone Malaguti 3, Gerardo Valentino 4 , Maddalena Auriemma5 , *Detailed experimental and numerical investigation of the spray structure in a GDI high-pressure swirl injector , Paper ID ICLASS06-189, ICLASS-2006 Aug.27-Sept.1, 2006, Kyoto, Japan.*
- [5] Padmesh Mandloi, Jayesh Mutyal, Pravin Rajeshirke elik and Blent zdalyan , *Numerical Spray Calibration Process , ILASS Americas, 23rd Annual Conference on Liquid Atomization and Spray Systems, Ventura, CA, May 2011,*
- [6] Wim Vandenberghe, Jorge Martins, Senhorinha F. C. F. Teixeira, Ricardo Falcao , *Use of fluent for the development of a DI-SI engine , ASME 2010 International Mechanical Engineering Congress & Exposition November, 12-18, 2010, Vancouver, British Columbia, Canada, IMECE2010-40881,*

- [7] Dennis N. Assanis, Sang Jin Hong, Akihiro Nishimura, George Papageorgakis1 Bruno Vanzielegem , *Studies of Spray Breakup and Mixture Stratification in a Gasoline Direct Injection Engine Using KIVA-3V* , S0742-4795 00!00303-3,
- [8] D.A. Kennaird, C. Crua, J. Lacoste and M.R. Heikal , *In-Cylinder Penetration and Break-Up of Diesel Sprays Using a Common-Rail Injection System* , 2002-01-1626.
- [9] David James MacMillan , *MEng., Influences on the Cold Start Behaviour of a Diesel Engine at Reduced Compression Ratio* , Submitted to the University of Nottingham for the degree of Doctor of Philosophy, May 2009
- [10] B. Bougie M. Tulej T. Deier N.J. Dam J.J. Ter Meulen . Gerber , *Optical diagnostics of diesel spray injections and combustion in a high-pressure high-temperature cell* , *Appl. Phys. B* 80, 10391045 (2005)
- [11] Tanisha Latrina Booker , *Characteristics Of Hydrogen Combustion In A Direct Injected Constant Volume Combustion Chamber Using Rainbow Schlieren Deflectometry* , Submitted in partial fulfillment of the requirements for the degree of Doctor of Philosophy, Tuscaloosa, Alabama 2011,
- [12] K. Al-Hakim, G. Wigley And A. G. F. Stapley , *Phase Doppler Anemometry Studies Of Spray Freezing* , 02638762/06/\$30.00+0.00 # 2006 Institution of Chemical Engineers [www.icheme.org/cherd](http://www.icheme.org/cherd) Trans IChemE, Part A, December 2006 DOI: 10.1205/cherd06014 *Chemical Engineering Research and Design*, 84(A12): 11421151,
- [13] J. Willneff , *3d Particle Tracking Velocimetry Based On Image And Object Space Information* , Institute of Geodesy and Photogrammetry, Swiss Federal Institute of Technology, 8093 Zurich, Switzerland, [willneff@geod.baug.ethz.ch](mailto:willneff@geod.baug.ethz.ch) Commission V, ICWG V/III,
- [14] Huihe Qiu and Chin Tsau Hsu , *Method of phase-Doppler anemometry free from the measurement-volume effect* , 1999 Optical Society of America OCIS codes: 010.3920, 290.0290, 290.4020, 290.5850, 350.4990,
- [15] Guillaume de Sercey , *Laser Induced Fluorescence for the measurement of air-to-fuel ratio's in Gasoline direct Injection engines* , PhD 2004,
- [16] Reitz RD , *Atomization and other Breakup Regimes of a Liquid Jet.* , Ph.D. Thesis,(1978)
- [17] Reitz RD, Bracco FV , (1986) *Mechanisms of Breakup of Round Liquid Jets* , *Encyclopedia of Fluid Mechanics*, Gulf Pub, NJ, 3, pp 233249,

- [18] Ohnesorge W , *Die Bildung von Tropfen an Dsen und die Auflsung flssiger Strahlen. Zeitschrift fr angewandte Mathematik und Mechanik* , Bd.16, Heft 6, pp 355358,(1931)
- [19] Wierzba A , *Deformation and Breakup of Liquid Drops in a Gas Stream at Nearly Critical Weber Numbers. Experiments in Fluids* , vol 9, pp 5964,(1993)
- [20] Arcoumanis C, Gavaises M, French B , *Effect of Fuel Injection Process on the Structure of Diesel Sprays* , SAE paper 970799,(1997)
- [21] Stegemann J, Seebode J, Baltes J, Baumgarten C, Merker GP (2002) , *Influence of Throttle Effects at the Needle Seat on the Spray Characteristics of a Multihole Injection Nozzle* , ILASS-Europe 2002, Zaragoza, Spain,
- [22] Reitz RD , *Modeling Atomization Processes in High-Pressure Vaporizing Sprays. Atomization and Spray Technology* , 3, pp 309337(1987) ,
- [23] ORourke PJ, Amsden AA , *The TAB Method for Numerical Calculation of Spray Droplet Breakup* ,SAE-paper 872089,(1987)
- [24] *Fluent 6.3 User's Guide, September 2006*
- [25] R. Steiner, C. Bauer, C. Kruger, F. Otto, and U. Maas. , *3d-simulation of diesel combustion applying a progress variable approach accounting for complex chemistry* , SAE paper, (SAE 2004-01-0106), March 2004.
- [26] *Student Chemical Database*
- [27] Kume, T., Iwamoto, Y., Iida, K., Murakami, M., Akishino, K., and Ando, A., 1996, *Combustion Control Technologies for Direct Injection SI Engine* ,SAE Paper 960600.
- [27] Hiroyasu, H., and Arai, M *Structure of Fuel Sprays in Diesel Engines* ,Transactions of the SAE Vol 99,Sect 3, pp 1050-1061, 1990.